Synthesis and property measurements of thermoelectric materials

Chapter 1

Synthesis and property measurements of thermoelectric materials

PAZ VAQUEIRO*

Department of Chemistry, University of Reading, Reading, RG6 6AD, UK

*E-mail: p.vaqueiro@reading.ac.uk

Abstract

Research in thermoelectric materials involves the synthesis, structural characterisation and measurement of thermal and electronic transport properties. It spans the fields of solid-state chemistry, condensed matter physics, materials science and engineering. This chapter provides an introduction, accessible to those with little prior experience in the field, to the synthetic approaches used for the preparation of thermoelectric materials, and to the measurement techniques employed for the characterisation of their transport properties. Methods for the preparation of powder and single-crystal samples are presented, together with the processes commonly used for the consolidation of samples into well-densified ingots. The measurement techniques for the properties required for the determination of the thermoelectric figure of merit, *ZT*, are described, together with their limitations and possible sources of error. Alternative approaches for the direct determination of *ZT* are also outlined, together with Hall coefficient measurements, reflecting the importance of charge-carrier concentration and mobility to the detailed understanding of thermoelectric materials.

1.1 Introduction

Thermoelectric modules are solid-state devices composed of pairs of *n*- and *p*-type thermoelectric materials, which enable conversion of heat into electrical power. This property could therefore be exploited for energy recovery from waste heat. The physical basis of thermoelectric power generation is the Seebeck effect: when a material is subjected to a temperature gradient, an electrical potential is generated. Hence, when *n*- and *p*-type thermoelectric materials are paired in a couple (Figure 1.1) and a temperature gradient is applied, electrons and holes conduct heat from the hot to the cold junction, and an electrical current is generated. For power generation, the maximum efficiency of a thermoelectric module, consisting of a series of couples of two materials, A and B, is given by the expression:[1]

[Figure 1.1 near here]

$$\phi = \frac{T_H - T_C}{T_H} \frac{\sqrt{1+Z_c\bar{T}}-1}{\sqrt{1+Z_c\bar{T}}+T_C/T_H} \qquad (1.1)$$

where T_H and T_C are the temperatures at the hot and the cold junctions, respectively and $\bar{T}$ is the average temperature:

$$\bar{T} = \frac{T_H+T_C}{2} \qquad (1.2)$$

and Z_c is the figure of merit of the couple. This is dependent on the Seebeck coefficient, S, electrical resistivity, ρ, and thermal conductivity, κ, of the materials A and B:

$$Z_c = \frac{(S_A-S_B)^2}{\left[(\rho_A\kappa_A)^{1/2}+(\rho_B\kappa_B)^{1/2}\right]^2} \qquad (1.3)$$

Therefore, the thermoelectric power generation efficiency depends on the Carnot efficiency ($\Delta T/T_H$) and the properties of the materials A and B (i.e. Z_c). The efficiency can therefore be improved by either increasing the temperature gradient or by increasing Z_c.

The urgent need to reduce the dependency on fossil fuels has stimulated considerable research efforts for the discovery of materials with better properties, to improve the efficiency of thermoelectric power generation. To facilitate the optimisation of individual thermoelectric materials, the dimensionless figure of merit (*ZT*) of a material is defined as:

$$ZT = \frac{S^2 T}{\rho \kappa} = \frac{S^2 \sigma T}{\kappa} \qquad (1.4)$$

where σ is the electrical conductivity (which is the inverse of the electrical resistivity), and $S^2\sigma$ is known as the power factor. To estimate the efficiency of a thermoelectric device, Z_c may be approximated as the average Z for the *n*- and *p*-type materials forming the couples. Measurements of electronic and thermal transport properties are essential to determine Z_c and therefore of utmost importance for the development of better thermoelectric materials.

Research in thermoelectric materials entails synthesis, structural characterisation over a wide range of length scales and the study of thermal and electronic transport in a broad class of materials, and spans the fields of solid-state chemistry, condensed matter physics, materials science and engineering. The classes of inorganic materials currently under investigation, which have been reviewed elsewhere,[2,3] include chalcogenides,[4,5] oxides,[6] oxychalcogenides,[7,8] and intermetallic phases such as clathrates,[9,10] half-Heusler[11] and Zintl phases.[12] Recent progress in selected examples on materials is described elsewhere in this volume. This chapter aims to provide an introduction, accessible to those with little experience in the field, to the approaches used for the synthesis of thermoelectric materials, and to the measurement techniques employed for the characterisation of their transport properties.

1.2 Synthesis

Synthesis is the first essential step in the production of thermoelectric materials. The traditional methods for the preparation of inorganic thermoelectric materials require high temperatures and produce bulk materials with large particle sizes. In recent years, new approaches, such as mechanochemical, solvothermal and colloidal synthetic methods have developed greatly. These alternative methodologies facilitate the production of nanostructured materials, which are very attractive, given that nanostructuring can be a highly-effective approach to increase the thermoelectric figure of merit.[13] The growth of single crystals is also important as it facilitates the investigation of the anisotropy of the physical properties, which can in turn be exploited to optimise thermoelectric performance. A variety of approaches, ranging from the well-established Czochralski and Bridgman methods to more exploratory methodologies using fluxes or chemical vapour transport, are currently used to grow single crystals of thermoelectric materials. A practical overview of the synthesis techniques identified above, together with examples of their application to relevant thermoelectric materials, is presented here.

1.2.1 High-temperature synthesis

High-temperature synthesis, often termed the ceramic method, entails heating of components at elevated temperatures for an extended period of time.[14,15] For instance, the syntheses of Bi_2Te_3, the skutterudite $CoSb_3$ and $Na_2Co_2O_4$ can be carried out through the following reactions carried out at temperatures in excess of 1000 K for several hours.[16,17,18]

$$2\ Bi + 3\ Te \rightarrow Bi_2Te_3 \qquad (1.5)$$

$$Co + 3\ Sb \rightarrow CoSb_3 \qquad (1.6)$$

$$Na_2CO_3 + 2/3\ Co_3O_4 \rightarrow Na_2Co_2O_4 + CO_2(g)\ (\text{in air}) \qquad (1.7)$$

Reactions between solid-state materials are generally slow and require high temperatures, because they depend on atomic diffusion, which increases with increasing temperature. High temperatures are necessary for sufficient atomic diffusion to take place to enable reaction to occur. If we consider two particles of the elemental solid reagents A and B, in close contact with each other, the reaction to form product AB requires atomic diffusion of A into B and vice-versa (Figure 1.2). As the reaction progresses, the product AB is formed at the boundary between A and B, and further reaction requires diffusion of A and B through the product. As the thickness of the product layer increases, the reaction rate will slow, since the product layer acts as a barrier for further diffusion of A into B and B into A. Therefore, in order to reduce reaction times, reagents should be ground to reduce the particle size and ensure intimate mixing, to maximise the contact area. For the same reason, reaction mixtures are often pressed into pellets prior to heating, and samples are removed periodically from the furnace and reground, in order to create new interfaces where reaction can occur. Grinding and reheating two or more times is often required before a phase-pure product is obtained. While the reactants are usually solids at room temperature, they may melt or even volatilise at the temperatures required for the reaction to occur. For instance, tellurium and antimony melt above 723 and 900 K, respectively, while sulphur becomes a gas above 718 K. As the atomic diffusion rate is higher for liquid or gaseous phases, this will usually aid the reaction. However, phase diagrams should be consulted (when available) to decide on the heating conditions. Compilations of phase diagrams are available,[19] as well as online databases such as ACerS-NIST PHASE4.4, the Landolt-Börnstein database (also known as SpringerMaterials) and the ASM Alloy Phase Diagram Database. If phases that melt incongruently are formed on heating, phase segregation may occur on cooling. Under those circumstances, quenching of the melt may be required, or ball milling (Section 1.2.2) may be a more suitable synthetic approach.

[Figure 1.2 near here]

Heating of reaction mixtures at temperatures up to 2100 K can be achieved using furnaces that operate by resistance heating. Metallic alloys are used as the heating elements in furnaces operating at temperatures up to 1500 K, while ceramic elements are used for higher temperatures: silicon carbide elements can operate up to 1900 K, and molybdenum disilicide elements can reach temperatures of 2100 K. Furnaces that use radio-frequency (RF) induction coils for heating can also be employed. Higher temperatures, up to 3300 K can be achieved by arc melting, which heats by passing an electric arc through the reagents, causing them to melt. Arc melting is a particularly convenient method for the preparation of Heusler and half-Heusler phases,[20] because this class of thermoelectric material contains chemical elements with very high melting points. A detailed description of the design and working principles of different types of furnaces is given by Motzfeldt.[21]

While preparation of oxides is often carried out by heating in air, this is not suitable for the synthesis of chalcogenides or intermetallic phases, which would rapidly oxidise under those conditions. Horizontal tube furnaces can be used to heat reaction mixtures under a flowing gas, with a bubbler attached to the exit to maintain a positive pressure and prevent back diffusion of air. This enables reactions to be carried out under an inert (e.g. N_2 or Ar), oxidizing (O_2) or a reducing (e.g. H_2/Ar mixture) atmosphere, as well as syntheses involving reactive gases to be performed. For instance, sulfides can be prepared in a tube furnace by flowing H_2S or CS_2 mixed with an inert gas, as exemplified by the quaternary sulfide $ACuMnS_2$ (A = K, Rb, Cs), prepared by reacting A_2CO_3, MnS and CuO under flowing CS_2/N_2, at 1000 K.[22] As both H_2S and CS_2 are highly toxic, caution is required when carrying out such reactions.

A major disadvantage of reactions under a flowing gas is that changes in stoichiometry may occur due to transport of volatile components. For this reason, the evacuated sealed tube method (Figure 1.3) is quite commonly used for the synthesis of chalcogenides, oxychalcogenides and intermetallic phases. This entails loading the reaction mixture into a tube made of heat-resistant glass (borosilicate or fused silica, depending on the reaction temperature), which is evacuated using a vacuum line and sealed using a gas-oxygen torch,[23] prior to heating it in a furnace. To reach the temperatures required to seal heat-resistant glass, the gas-oxygen torch will burn a mixture of natural gas (or propane) and oxygen. The reactions described in Eq. (1.5) and (1.6) are performed using this method. When using sealed glass ampoules, the melting and boiling points of reactants must be considered: reagents that volatilize on heating may cause sealed ampoules to explode due to an increase in internal pressure, while reactants that melt may attack the glass, and therefore destroy the ampoule. Prior to raising the temperature to the reaction temperature, it is advisable to heat reaction mixtures for a few hours below the melting or boiling point of any reactant, to enable it to react with the other components, in order to minimise the risk of damage to the sealed ampoule.

[Figure 1.3 near here]

As the products of solid-state reactions cannot be easily purified, the purity of the reagents must be assessed thoroughly, to ensure that the initial reaction mixtures have the intended stoichiometry. It should never be assumed that the composition of a reagent is that stated by the supplier. The reagent purity given by the supplier is usually expressed in terms of “trace metal basis”. This neglects the possible presence of elements such as oxygen or carbon. Moreover, depending on how reagents are stored, they can with time oxidise, or absorb moisture or CO_2 from air. For instance, rare-earth oxides stored in air often contain carbonates. Purification of reagents may be required prior to use. For example, heating in air

is required to remove carbonates from rare-earth oxides, while heating under a reducing atmosphere (e.g. H_2/Ar) may be required to remove oxides from germanium metal prior to use. Traces of oxides from metals such as sodium or barium, which should be stored under an inert atmosphere, can be eliminated by mechanically removing the outer surface inside a glovebox.

Another frequent source of problems is the container used for high-temperature reactions, as it may lead to contamination of the sample. Ideally, reaction containers must be inert, to avoid reaction with the reactants and products, and must also be able to withstand elevated temperatures. Crucibles and boats can be made of a variety of materials, including alumina, fused silica, graphite or platinum. The maximum operating temperatures of common crucible materials, under different atmospheres, are summarised in Table 1.1. When choosing a crucible, it is essential to ensure that it is chemically compatible with the reaction mixture it will contain. For example, antimony, bismuth, selenium and tellurium all react quite readily with a platinum crucible on heating, while alkali or alkaline-earth metals, titanium or aluminium will attack fused-silica containers at elevated temperatures. To avoid attack on the container, reactions using the evacuated, sealed-tube method, may sometimes require the inside of the fused-silica tube to be coated with carbon, which can be achieved by pyrolysis of acetone or toluene. For very reactive reaction mixtures, it may be necessary to place a graphite or boron-nitride crucible inside the glass ampoule, or to use a welded niobium or tantalum tube, to contain the reaction mixture.

[Table 1.1 near here]

1.2.2 Mechanochemical synthesis

Mechanochemical synthesis, usually implemented in a ball mill, is an increasingly popular method for the preparation of thermoelectric materials, as well as many other classes of

organic or inorganic material.[24,25,26] The term mechanochemistry, which was first introduced by Ostwald,[27] refers to chemical reactions that are induced by mechanical energy,[28] instead of heat (thermochemistry) or light (photochemistry). The first mention of a mechanochemical reaction, milling of HgS with copper to produce elemental mercury, appears to have been made by a disciple of Aristotle, Theophrastus of Eresus, around 315 BC.[29] The establishment of mechanochemistry as a distinct branch of chemistry at the end of the 19th century is sometimes attributed to Matthew Carey Lea, who demonstrated that silver and mercury halides react differently when exposed to heat or to a mechanical action.[30]

Mechanochemical synthesis can promote fast reactions between solids (or between a solid and a gas, for instance for the synthesis of hydrides[31]), resulting in reduced reaction times. In mechanochemical reactions, high-energy impact collisions result in pulverisation, cold welding and re-welding of the grains, and introduce defects, disorder and strain within the crystallites, often leading to the formation of amorphous phases.[32] A number of theories and models for mechanosynthesis have been developed over the years, and these have been reviewed by Baláž.[33] The *hot-spot* theory proposes that friction or impact between powder particles generates high local temperatures, of over 1000 K, for 10^{-3}-10^{-4} seconds, on surfaces of around 1 μm^2,[34] while the *magma-plasma* model postulates that a special plasmatic state is formed at the spot where particles collide, which locally reaches temperatures of *ca.* 10000 K.[35] However, such high temperatures are unlikely to be reached when organic components are involved, as decomposition would occur. In such cases, a mechanism involving the diffusion of reactants through a mobile phase, which may be a gas, eutectic liquid or amorphous solid, has been suggested.[26] Some mechanochemical reactions (e.g. synthesis of metal nitrides or sulfides) proceed through an exothermic self-propagating reaction, in which ignition occurs when the powder is activated by milling due to grain size reduction and defect formation.[36] Ignition results in an abrupt increase of the temperature of the reaction mixture.

[Figure 1.4 near here]

There are different types of mills for mechanosynthesis (Figure 1.4), but all of them adopt the same basic operating principle: the powdered reagents are placed in a sealed jar, together with small balls, which are used to crush and grind the sample. In planetary ball mills, which are the most commonly used type for the synthesis of thermoelectric materials, milling entails planetary-like movement of the jars, which rotate in the opposite direction to the supporting disc. Attrition mills consist of a cylindrical chamber with a central rotating shaft that has impellers. The rotating shaft and impellers create a stirring motion in the powder and balls, causing mixing and grinding. In vibration (shaker) mills, grinding occurs by rapid linear oscillation of the jars, at frequencies of 10-30 Hz. Parameters such as the ball-to-powder ratio, the degree of filling and the milling time and speed are usually varied to optimise the synthesis of materials. To avoid oxidation of air-sensitive reagents or products, milling is usually performed under an inert atmosphere, and the jar is loaded and sealed inside a glovebox. Alternatively, gas-tight jars that can be purged with the desired gas are commercially available. The balls and jars are either made of metal (stainless steel or hardened steel) or a ceramic material (such as agate, zirconia or tungsten carbide), and when choosing a container, consideration must be given to the possible contamination and reaction of the powdered sample with the jar and grinding balls. Care must also be taken when opening jars after milling, as finely-ground metal powders could spontaneously ignite and cause a fire when exposed to air.

[Table 1.2 near here]

As illustrated in Table 1.2, mechanosynthesis has been successfully exploited for the preparation of a wide variety of thermoelectric materials, including Si-Ge alloys,[37] tellurides,[38,39,40] sulfides,[41,42,43] skutterudites,[44,45] half-Heusler compounds[46] and

oxychalcogenides.[47] Ball milling can produce either the desired phase in a poorly crystalline form, or a finely ground precursor, which will convert into the desired phase following reactive hot pressing or spark-plasma sintering (SPS), described in section 1.3. For example, the preparation of Cu_5FeS_4 by ball milling results in the formation of a poorly crystalline phase together with unreacted iron (Figure 1.5), and hot pressing is required to produce highly crystalline Cu_5FeS_4.[43] By contrast, filled skutterudites such as $Ce_{0.8}Fe_3CoSb_{12}$ or $Ce_{0.5}Yb_{0.5}Fe_{3.25}Co_{0.75}Sb_{12}$ form directly on milling.[44]

[Figure 1.5 near here]

Ball milling can also be exploited as a top-down approach to reduce the particle size in order to produce nanopowders. This is desirable as nanostructuring can lead to a substantial reduction in lattice thermal conductivity due to increased phonon scattering by interfaces.[13] For example, ball milling of bulk $Bi_{0.5}Sb_{1.5}Te_3$ to produce nanoparticles with an average particle size of 20 nm, results in a nanostructured material that exhibits a peak figure of merit, ZT = 1.4 at 373 K, due to the reduction in thermal conductivity.[48] However, ball milling to produce nanopowders can sometimes lead to contamination, or to the formation of oxides on the highly-reactive particle surfaces, which degrades the overall thermoelectric performance, as exemplified by a study of the type I clathrate $Ba_8Cu_{4.5}Si_6Ge_{35.5}$.[49] The consolidation process, which must be fast to avoid grain growth when sintering, is critical for nanopowders, with SPS being usually favoured (Section 1.3.2). Ball milling is also often exploited as a top-down approach for the preparation of nanocomposites by mechanical mixing. For example, Li *et al*. achieved a ZT = 1.33 at 373 K by preparing a composite of $Bi_{0.3}Sb_{1.7}Te_3$ with 0.4 vol% SiC nanoparticles.[50] The scalability of mechanochemical synthesis has been investigated by Baláž and co-workers, who have successfully produced materials such as tetrahedrite and Cu_2ZnSnS_4 using an industrial eccentric vibratory ball mill.[51,52] This type of mill can be used to produce batches of up to 50 kg of material.

1.2.3 Single-crystal growth

Single crystals are needed to investigate the intrinsic properties of thermoelectric materials and are particularly useful when their properties show marked anisotropy. The Czochralski method[53] and the Bridgman technique[54] have been applied for the growth of large single crystals, while smaller crystals may be grown using fluxes[55,56,57] or by chemical vapour transport.[14,58] In the Czochralski method (Figure 1.6(a)), a single crystal is grown by dipping a seed crystal into a melt of the feed material. The seed crystal is attached to a moveable rod, which is slowly pulled, while rotating, from the melt. This causes the melt to crystallize at the interface between the seed and the melt, slowly growing a crystal. Crystal growth by the Czochralski method is affected by parameters such as the temperature gradient, pulling rate, the crucible materials and the reaction atmosphere. A detailed discussion of this technique has been provided by Hurle.[59] Examples of thermoelectric materials that have been successfully grown using this method include Bi_2Te_3 alloys,[60] $Si_{1-x}Ge_x$,[61] and clathrates such as $Ba_8Ga_{16}Ge_{30}$.[62] Although the Czochralski method enables the growth of large, high-quality crystals, with diameters of the order of 50 mm, it is slow (growth rate of a few mm h^{-1}) and the growing equipment is expensive.

[Figure 1.6 near here]

The Bridgman method involves slow movement, typically vertical, of a crucible containing a melt of the feed material between a high- and a low-temperature zone (Figure 1.6(b)). The low-temperature and high-temperatures zones respectively are set to a temperature below and above the melting point of the material being grown. The crucible is typically made of fused silica, and has a cylindrical shape with a sharp conical tip. When the melt is slowly lowered into the colder region, a crystal starts growing in the conical tip, although a seed crystal may

also be used. The crystal growth rate is in the range 0.1-30 mm h^{-1}. The Bridgman method is widely available, with examples of crystals of thermoelectric materials grown by this method that include $Bi_2Te_{3-x}Se_x$,[63] SnSe,[64] the skutterudite $CoSb_3$,[65] Mg_2Si[66] and the clathrate $Ba_8Cu_{14}Ge_6P_{26}$.[67]

The Czochralski and Bridgman methods work well for materials that melt congruently (i.e. the composition of the melt is identical to the composition of the solid). For materials that melt incongruently, alternative approaches can be adopted. In the flux method,[55,56,57] a molten solid, which can be a low melting-point salt or a metal, is used as solvent. The reagents and the flux are heated until the flux melts and reagents dissolve in the flux. On cooling, nucleation of crystals of the product occurs as the solution becomes supersaturated. The crystals can be separated from the flux by washing with a solvent that dissolves the flux, without destroying the crystals, or sometimes by centrifugation of the hot mixture. Crystals of up to 10 mm edge length can be grown in this way. Important considerations when choosing a flux are:[68]

(a) the reagents must be soluble in the flux, with the solubility changing significantly with temperature;

(b) the flux should not form stable compounds with the reagents (unless a reactive flux[56] is sought);

(c) the flux should have a reasonably low melting point, and low volatility and viscosity at the crystallisation temperature;

(d) the flux should not react with the crucible;

(e) the flux should be easily separated from the crystals; and

(f) use of toxic fluxes (e.g. mercury) should be avoided.

Examples of fluxes include eutectic LiCl/KCl or NaCl/KCl mixtures, with melting points of 625 and 931 K respectively,[55] metals such as Sn, Ga or In (melting points of 505, 303 and 430 K, respectively),[56] or polychalcogenide fluxes A_2Q/Q (where A is an alkali metal and Q, a chalcogen).[57] Halide or polychalcogenide fluxes can be easily removed by washing with water, while for instance a tin flux can be removed by washing with dilute hydrochloric acid. An introductory account of the practical aspects of crystal growth using fluxes, that focuses on oxides and intermetallics, has been given by Tachibana.[68] Selected examples of single crystals of thermoelectric materials[69,70,71,72,73] grown in this way are presented in Table 1.3.

[Table 1.3 near here]

Chemical vapour transport reactions, which were developed by Schäfer in the 1950s and 1960s,[74] involve a condensed phase which is volatilised in the presence of a gaseous transporting agent, and subsequently deposited in another region of the reaction vessel, often as single crystals. For example, single crystals of ZnS can be grown using I_2 as the transporting agent.[14] The transport reaction is carried out in an evacuated sealed ampoule, under a temperature gradient, which can be generated using a tube furnace with two independently-heated zones. For the transport reaction to occur, a mixture of solid ZnS and the transport agent are placed at the hot end of the tube, at 1173 K, while the other end is maintained at 1073 K. The vapour transport reaction can be described by the following equilibrium:

$$\mathrm{ZnS(s)} + \mathrm{I_2(g)} \leftrightarrows \mathrm{ZnI_2(g)} + \frac{1}{2}\mathrm{S_2(g)} \qquad (1.8)$$

where I_2, ZnI_2 and S_2 are all gases at the reaction temperature. This reaction is endothermic, and therefore according to Le Chatelier's principle, the partial pressures of ZnI_2 and sulphur will be lower at the colder end of the tube, where ZnS will recrystallise. Endothermic reactions will always transport from the hot to the cold region, while for exothermic reactions

transport will occur from the cold to the hot region. Common transporting agents, which have been discussed in detail by Binnewies *et al.*,[58] include Cl_2 and O_2 (auto transport following decomposition) for oxides, I_2 or HCl for chalcogenides, and I_2 or SiI_4 for silicides. Although chemical vapour transport has not been widely used for thermoelectric materials, crystals of a very large number of binary, ternary and even quaternary chalcogenides have been grown using this method.[58] For instance, chemical vapour transport, using $BiBr_3$ as transport agent,[75] produces single crystals of $Bi_{0.5}Sb_{1.5}Te_3$ while 20 mm long needles of the sulfide Cu_2CdGeS_4 can be produced using CdI_2.[76] Controlling the reaction conditions enables the growth of nanowires instead of larger single crystals, as exemplified by those of lead chalcogenides.[77] Thermoelectric silicides, can also be grown using this approach, and for example, single crystals of $MnSi_{1.73}$ and nanowires of $CrSi_2$ have also been reported.[78,79] Software to predict optimum reaction conditions for chemical vapour transport is available,[80] and extensive tables of previously-reported conditions for the growth of a large number of oxides, chalcogenides and intermetalics have been published.[58]

1.2.4 Solvothermal synthesis

Although solvothermal synthesis has traditionally been exploited for the growth of single crystals of a wide range of materials (e.g. quartz, zeolites, MOFs, metal oxides, metal chalcogenides), its main application in thermoelectrics is for the preparation of nanostructured powders. A solvothermal process is a heterogeneous reaction occurring in a sealed vessel and in the presence of a solvent heated above its boiling point and under pressure.[81,82] Under solvothermal conditions, it becomes possible to dissolve and crystallize materials that are insoluble at ambient temperature and pressure, due to changes in the physico-chemical properties of the solvent (viscosity, polarity, dielectric constant, etc.). For example, the viscosity of water decreases markedly with increasing temperature and pressure. This accelerates ion diffusion, and hence the solubilisation of the reactants and the growth of

the final product. When the solvent is water, the process is termed hydrothermal synthesis. A wide range of minerals grow in nature under hydrothermal conditions. The term solvothermal refers to the use of a non-aqueous solvent. Commonly-used solvents include liquid ammonia, methanol, ethanol, ethylene glycol or ethylenediamine.[83,84] Given that solvothermal reactions are performed in sealed vessels, the pressure-temperature behaviour of the solvent at constant volume becomes important,[82] with the solvent reaching supercritical conditions in some reactions. For example, for water, the critical temperature and pressure are 647 K and 221.2 bar, while NH_3 reaches the critical point at 405 K and 111 bar. Below those conditions, a liquid and a gas phase coexist, but above the critical point only one phase, the supercritical phase, exists.

[Figure 1.7 near here]

In order to carry out solvothermal reactions, vessels capable of containing a corrosive solvent at high temperatures and pressures are required. Small scale reactions can be performed using sealed thick-walled Pyrex ampoules (or borosilicate vials with Teflon caps for reactions under mild conditions). Due to its ease of use, the vessel most employed for solvothermal reactions is the general-purpose autoclave (Figure 1.7), which consists of an inner Teflon cup and lid, enclosed in an outer stainless-steel body. The capacities of these autoclaves range between 23 and 125 mL, with a recommended maximum filling of 2/3 of the total volume. Autoclaves suitable for heating in a microwave oven are also available. While the use of a Teflon liner provides inertness and avoids reactions with the metal container, it also limits the maximum operating temperature to *ca*. 523 K, as Teflon starts to deform above 473 K. Autoclaves capable of operating at higher temperatures and pressures have been described in detail by Byrappa and Adschiri.[81]

[Table 1.4 near here]

Solvothermal methods have been used to prepare thermoelectric materials such as Bi_2Te_3,[85,86] $Bi_xSb_{2-x}Te_3$,[87] PbTe,[85,88] Cu_2Se,[89] $Sn_{1-x}Se$,[90] $CoSb_3$[91] and $FeSb_2$[92] (Table 1.4), with different sizes and morphologies. Surfactants and polymers are sometimes used as additives to control the morphology. Most of these solvothermal reactions involve redox processes. While metal cations (e.g. Bi^{3+}, Pb^{2+}) may remain in their initial oxidation state, the chalcogen sources usually undergo a reduction. For instance, when Te and SeO_2 are used as chalcogen sources, the following reductions occur:

$$Te + 2e^- \rightarrow Te^{2-} \qquad (1.9)$$

$$Se^{4+} + 6e^- \rightarrow Se^{2-} \qquad (1.10)$$

Reducing agents, such as hydrazine and sodium borohydride are added, when reactions with large reduction potentials are involved. In other cases, the solvent plays a role in the redox processes. Amines and alcohols such as oleylamine and ethylene glycol often act as weak reducing agents. It is also known that sulfur readily dissolves in ethylenediamine and liquid ammonia, producing highly reactive species through a disproportionation process.[93,94] Alternatively, the decomposition of compounds such as thiourea or thioacetamide has been used to generate sulfide anions *in-situ*.[95,96]

Although solvothermal synthesis provides a good degree of control over the particle size and morphology, the control over the stoichiometry of the final product may be more limited. Controlling the charge-carrier concentration through the introduction of dopants can also be challenging, as the composition of the final product may differ from that of the initial reaction mixture. The few studies describing the synthesis of doped thermoelectric materials using a solvothermal method, include lead doping in Cu_2Se,[97] Cu_3SbSe_4[98] and SnSe,[99] and copper doping in SnSe.[100] Moreover, to ensure that well-densified ingots are produced, complete removal of solvent, surfactants and any soluble products from the surface of the nanoparticles

is required. This may require extensive washing, followed by heating in vacuum or under an inert atmosphere,[98] which may lead to nanoparticle growth. A potential application of solvothermal synthesis is in the preparation of nanocomposites, either by coating a bulk material with nanoparticles,[101] or by preparing nanoparticles which are then mechanically added to a bulk material.[102]

1.2.5 Colloidal synthesis

Solution-based approaches enable simultaneous growth of large numbers of nanoparticles with narrow size and shape distributions and are therefore of interest for the preparation of nanostructured thermoelectric materials.[103] The colloidal synthesis method, which entails the reaction of precursors in a high boiling-point organic solvent, in order to produce a colloidal suspension of nanoparticles, has been extensively developed for the preparation of metal and chalcogenide nanoparticles.[104,105,106] In this method, which can be carried out by a "heat-up" or a "hot-injection" technique (Figure 1.8), nanoparticles are produced through rapid nucleation followed by a growth process, with subsequent isolation from the reaction mixture and extensive washing. Reactions are typically carried out in an oxygen-free environment, using a three-neck round-bottom flask connected to a condenser and Schlenk line, allowing purging with an inert gas. Colloidal synthesis can involve redox reactions, although it often entails thermal decomposition of organometallic precursors.[104] For example, $CoSb_3$ can be prepared by a modified polyol "heat-up" method, using sodium borohydride as a reducing agent for $SbCl_3$,[107] while the synthesis of CdSe[108] entails the injection of the organometallic precursor dimethyl cadmium and trioctylphosphine selenide directly into a hot solvent, with thermal decomposition resulting in rapid nucleation and subsequent growth to generate CdSe nanoparticles. Commonly-used precursors for the synthesis of chalcogenide nanoparticles include tertiary phosphine chalcogenides (e.g. trioctylphosphine selenide) or alkylamine-chalcogenides (e.g. oleylamine-sulphur), which are produced *in situ* by dissolving the

chalcogen in a phosphine or an alkylamine.[109] Phosphines and amines also act as surface ligands, coordinating to the surfaces of the nanoparticles once formed, to stabilize them and prevent Ostwald ripening.[106] Hard-soft-acid-base theory provides guidance on the selection of suitable ligands for cations and chalcogens.[106,109] Thermoelectric chalcogenides such as $Bi_2Te_{3-x}Se_x$,[110] PbTe/PbS and PbS/Ag nanocomposites,[111,112] Cu_2SnSe_3,[113] $Cu_2CdSnSe_4$[114] and SnSe[115,116] have been prepared by colloidal synthesis (Table 1.5). The synthesis of nanoparticles of intermetallic compounds is significantly less developed. Metal alkyamides $M(NR_2)_n$ and silylamides $M[N(SiMe_3)_2]_n$, although offering potential as precursors for metal and metalloid nanoparticles, are both expensive and extremely air and moisture sensitive, due to their high reactivities. Amides, which can be formed *in-situ* by reaction of metal chlorides with long-chain primary or secondary amines in the presence of a strong Brønsted base, have been proposed as precursors for the synthesis of monodisperse nanoparticles of metals and metalloids such as In, Sn, Bi, Sb, Ga, Cu, Zn and binary compounds such as Cu_6Sn_5, Cu_2Sb and Bi_xSb_{1-x}.[117]

[Figure 1.8 near here]

[Table 1.5 near here]

As is the case with nanoparticles produced by solvothermal synthesis, removal of solvent, ligands and any soluble products from the surface of the nanoparticles is required prior to consolidation.[101] This may for instance be achieved by treatment with hydrazine,[118] although a widely used approach for the removal of organic impurities is annealing, which may result in particle growth, under an inert gas or vacuum.[101] Doping of nanoparticles produced by colloidal synthesis, to control the charge carrier concentration, is also challenging.[103] Strategies that have been adopted include the inclusion of a dopant precursor in the initial reaction solution, as exemplified by the synthesis of Sn- and Bi-doped Cu_3SbSe_4

nanoparticles.[119] It is also possible to replace a fraction of the cations from the starting nanomaterial with a new type of cation, through a partial ion-exchange process.[120] Alternatively, a dopant can be added, in the form of a salt, to the nanopowder to be consolidated.[106] An advantageous application of colloidal synthesis, may be for the production of inks for printing flexible thermoelectric devices.[103]

1.2.6 Precursor methods

Precursor methods are well developed for oxides, but there are very few examples of their use for other classes of thermoelectric materials. The use of precursors enables intimate mixing of the reagents, to facilitate atomic diffusion and reduce the temperature and time required for product formation, in comparison to the ceramic method (Section 1.2.1). Precursor methods can simply entail co-precipitation, as exemplified by the synthesis of $Ca_3Co_4O_9$, through precipitation of a precursor from an aqueous solution of calcium carbonate and cobalt nitrate, following the addition ammonium carbonate.[121] Heating of this precursor in air results in decomposition, producing the final product, $Ca_3Co_4O_9$. However, when using a co-precipitation method, it may be difficult to ensure that the precursor and therefore the final product have the desired stoichiometry, as not all cations will precipitate at the same pH value. This disadvantage may be avoided by using a sol-gel method,[122] in which a sol, consisting of a concentrated solution, or a stable suspension of colloidal particles of the reagents, is prepared. Gelation of the sol by concentrating it or maturing it, produces a gel, which can be described as a porous and continuous solid network surrounding a continuous liquid phase. The solid network in the gel is either an agglomeration of colloidal particles, or in polymeric gels, an aggregation and entanglement of polymer chains. Decomposition of the gel by heating, produces the final product.

Traditionally, the term “sol-gel” has been applied to syntheses employing metal alkoxides. In this case, a sol is formed through hydrolysis and condensation of alkoxide precursors, with

cross-linking resulting in the formation of a metal-oxane gel. However, more recently the term "sol-gel" has been extended to cover a wide range of chemistries, which have been discussed in detail by Danks and co-workers.[123] Five key types of gels have been identified in sol-gel chemistry:

(a) Colloidal gels, which consist of colloidal particles connected by van der Waals' interactions or by hydrogen bonding. A colloidal gel has for instance been used to produce Al-doped ZnO.[124]

(b) Metal-oxane polymer gels, which are inorganic polymers. An alkoxide sol-gel method has been used to prepare TiO_2 nanoparticles dispersed in $Ba_{0.22}Co_4Sb_{12}$.[125]

(c) Metal complex gels, which consist of weakly-bonded metal complexes. This involves the use of small molecules (often chelating), such as citric acid. For example, the citrate sol-gel method has been exploited for the synthesis of thermoelectric $Ca_3Co_4O_9$.[126]

(d) "Pechini" method gels, formed by *in-situ* polymerizable metal complexes. The Pechini method entails a transesterification between metal citrates and ethyleneglycol, to form an extended covalent network.

(e) Coordinating and cross-linking polymer gels. These contain polymers, such as alginate or polyvinylpyrrolidone, that can coordinate to metal cations.

Although sol-gel methods have been primarily developed for oxides, there are some approaches which are applicable to the synthesis of nitrides[127] and chalcogenides.[128,129] For instance, nitrides can be produced by ammonolysis of dialkylaminosilanes with ammonia, to form the sol, followed by condensation to make imide (–NH–) linkages and form a gel.[127] Sulfides can be made by an alkoxide sol-gel route, by replacing the hydrolysis by water which is used to produce oxides, with thiolysis with H_2S.[128,129] In the colloidal gel approach, metal chalcogenide nanoparticles are produced and then condensed to form a gel. [128,129]

Precursor or sol-gel methods have only rarely been used for non-oxide thermoelectric materials. Examples include the synthesis of Bi_2Te_3 or the skutterudite $CoSb_3$ by a co-precipitation route, followed by calcination and reduction under a hydrogen atmosphere.[130,131] Oxide precursors can also be reduced to intermetallic skutterudites by heating them on a magnesium bed, under an inert atmosphere.[132]

1.3 Consolidation

Following the synthesis of a thermoelectric material (Section 1.2), consolidation is generally required to produce dense ingots for property measurements. The consolidation of powders is achieved by sintering, which can be defined as "the extension of the contact area between powder particles in the solid state, by the transport of material across or around pores, under appropriate conditions of time, temperature, pressure, and atmosphere."[133] Sintering of crystalline materials occurs in three stages (Figure 1.9).[134] In the initial stage, adjacent particles bond through the formation and growth of contact areas between particles, but densification is limited. In the intermediate stage, significant densification occurs, and the contact areas between particles grow, but there is still a continuous network of pores. In the final stage, pore shrinkage and closure occurs, the remaining pores become isolated, and there is significant grain growth. The contact areas, also known as necks, grow mainly by atomic diffusion mechanisms, which are caused by gradients in vacancy concentration. In some cases, evaporation-condensation mechanisms or a liquid phase may also be involved in the growth of contact areas. The driving force for sintering is the reduction in surface area which occurs with increased densification. During the sintering process, the powder decreases its total surface free energy by reducing the total surface area. The densification rate increases with increased temperature and time, as well as with reduction in the particle size of the

‘green’ (unsintered) powder. Sintering is usually carried out at temperatures in the range of 67 to 80 % of the melting point of the solid.[135]

[Figure 1.9 near here]

In principle, cold pressing using a stainless-steel die, followed by annealing at high temperatures in a furnace, is the simplest approach to consolidate samples. In practice, this method often results in samples with low relative densities (with respect to the crystallographic density) and poor mechanical strength. Thermoelectric materials are usually consolidated by pressure-assisted sintering, using either hot pressing (HP) or spark-plasma sintering (SPS). Both methods are discussed below. The use of hot forging to increase the texture of thermoelectric materials will also be described.

1.3.1 Hot pressing

Hot pressing (HP) entails the application of a uniaxial external pressure while simultaneously heating the sample, although isostatic hot pressing, where the pressure is applied uniformly with a gas, can also be used.[136] HP increases the densification kinetics and, given that grain growth is not directly linked to the applied pressure, it can be used to limit grain growth, and to consolidate materials using lower sintering times and temperatures. While diffusion is the main densification mechanism in pressureless sintering, plastic deformation and creep can become major contributors under an applied pressure. A schematic representation of a uniaxial hot-press is shown in Figure 1.10. A die, which is usually made of graphite, is loaded with the powder to be consolidated, between two plungers. To facilitate the extraction of the sample after pressing, disposable graphite foil liners are often inserted. These can be placed on the top and bottom of the sample and also around the die walls. Pressure is applied while the die is heated, under vacuum or in a controlled atmosphere, using resistance heaters. Usually, the heating elements are located in the walls of the chamber where the die is

contained, and as a consequence, heating rates are low. Alternatively, the heat can be supplied by RF induction, to enable rapid consolidation and heating rates, comparable to those achieved by SPS.[137]

[Figure 1.10 near here]

The use of steel dies is not advisable, as steel deforms due to creep at high temperatures, and the powdered sample may also react with the steel at high temperatures. Under an inert atmosphere or vacuum, graphite will be stable at the temperatures required for the hot pressing of most thermoelectric materials. However, care should be taken to avoid the presence of air/oxygen, as graphite oxidises above 400ºC, and this can result in the release of carbon monoxide. As graphite can only withstand relatively low pressure loads before failure occurs, its use imposes a limit on the pressures that can be applied on the sample, which are typically between 0 and 100 MPa. Designs of dies capable of operating at higher pressures (up to 400 MPa), which would be suitable for HP and SPS, have inserts made of silicon carbide or tungsten carbide.[138,139] Alternatively, the use of dies made of carbon fibre-reinforced graphite has been suggested.[138]

HP can successfully produce ingots with densities above 97% of the theoretical (crystallographic) density, once the optimum conditions of temperature, pressure and time have been identified. Temperature is often the critical parameter that needs to be adjusted, because atomic diffusion increases exponentially with temperature. If the temperature is too high, sample decomposition, or changes in composition due to evaporation of more volatile elements, may occur. If the temperature is too low, the density of the ingot will be too low for transport property measurements (Section 1.4), and the mechanical strength of the ingot will also be poor. The effect of the atmosphere used during pressure-assisted sintering should also be considered. For instance, oxides consolidated under vacuum or a reducing atmosphere may have an increased concentration of oxygen vacancies.

1.3.2 Spark-plasma sintering

Spark-plasma sintering (SPS), also known as field-assisted sintering (FAST) or electric-current activated sintering (ECAS), differs from HP in the method used to heat the sample. In SPS, the mechanical loading system also acts as a high-power electrical circuit, and heating is achieved by passing a pulsed DC electrical current through the sample (if this is conductive) or through the die. The applied voltage, which is generally below 10 V, produces large currents, typically between 1-10 kA, resulting in efficient Joule heating and therefore extremely fast heating rates, of up to 1000 K min^{-1}. SPS enables significant reductions in the total duration of the sintering process to be achieved. This offers the benefit of reducing grain growth, a particularly desirable feature when consolidating nanopowders. A schematic diagram of an SPS system, highlighting the similarities and differences between HP and SPS is shown in Figure 1.10(b). Despite its name, there is no evidence of the presence of a plasma during the SPS process.[140] There are a number of comprehensive reviews on SPS.[141,142,143,144]

Most materials can be consolidated equally well by HP or by SPS. For instance, both approaches are suitable for obtaining well-densified $Ca_3Co_4O_9$ ceramics,[145] or Na-doped PbTe,[146] although differences in the microstructure may result in slightly different thermoelectric performances. For colusite ($Cu_{26}V_2Sn_6S_{32}$), Guilmeau and coworkers have shown that hot pressing at 1023 K produces an improvement of around 300 % in the figure of merit at 675 K, in comparison to SPS at 873 K.[147] This has been attributed to the formation of disordered domains and sulfur volatilisation due to the higher temperature used for HP processing.

There are some specific issues related to the nature of the heating in SPS that need to be considered. For electrically-conductive materials, the flow of electrical current through the powder will not occur homogeneously; instead it will depend on the packing of particles in

the unsintered body. This will result in the formation of local hot spots, and this local variation in temperature may influence the final microstructure of the consolidated material, which can sometimes show a current percolation pattern.[141] Moreover, for thermoelectric materials, the flow of a DC current through the powder during the SPS process may result in uneven heating, due to the Peltier effect, and hence large differences in grain size between the top and bottom faces of the consolidated sample can occur. Peltier heating or cooling occurs if there is a discontinuity in the Peltier coefficients of two materials in contact. As semiconductors have much higher Peltier coefficients than the electrodes and the die, Peltier heating or cooling will occur at those interfaces. It has been estimated that for semiconductors, Peltier heating can reach up to 10% of the total heating delivered by SPS.[141]

The large DC currents used in SPS may also drive the transport of mobile ions, resulting in inhomogeneous samples, with compositional gradients. For example, transport of Li^+ ions occurs when sintering $Li_{1.3}Fe_{0.3}Ti_{1.7}(PO_4)_3$ by SPS. This results in a colour gradient between the opposite faces of the consolidated ingot due to compositional changes and partial decomposition of the material.[148] The diffusion of Na^+ ions under SPS conditions has been used to produce the intermetallic clathrate $Na_{24}Si_{136}$ from a Na_4Si_4 precursor.[149] Given the known issues of degradation of phonon-liquid electron-crystal (PLEC) thermoelectric materials under a DC electric current,[150] diffusion of Cu^+ ions may also occur during the consolidation of materials such as $Cu_{2-x}S$ or $Cu_{2-x}Se$ by SPS. This however does not appear to have been investigated.

1.3.3 Hot forging

Many thermoelectric materials have highly anisotropic properties[64,151,152,153] and therefore, for polycrystalline samples, preferential alignment of the crystallites along a favourable transport direction can be exploited to enhance the figure of merit. As shown in Table 1.6, there can be rather large variations between the in-plane and the out-of-plane electrical resistivities, while

the anisotropy in the Seebeck coefficient is often less marked. Hence, alignment along the direction with the lowest electrical resistivity should be advantageous. One of the most straightforward approaches to induce preferential orientation is that of hot forging, which entails repeated consolidation of the ingot by HP or SPS, using dies with progressively larger diameters (Figure 1.11). Following hot forging, comparison of the X-ray diffraction pattern of the consolidated ingots with that of a randomly-oriented powder sample, through the calculation of the Lotgering factor, *F*, can be used to assess the degree of texture.[154] In the Lotgering method the orientation factor is defined as:

$$F = \frac{p - p_0}{1 - p_0} \qquad (1.11)$$

where

$$p = \frac{\sum I(00l)}{\sum I(hkl)} \qquad (1.12)$$

$I(00l)$ and $I(hkl)$ are the measured intensities of reflections with (00*l*) and (*hkl*) Miller indices, and p_0 is the value of p for a randomly oriented powder. The orientation factor takes a value $F = 0$ for a randomly-oriented sample, and $F = 1$ for a fully oriented or textured sample.

[Table 1.6 near here]

[Figure 1.11 near here]

Hot forging has been investigated for a number of thermoelectric materials. For example, a 22% improvement in the maximum figure of merit of *n*-type $Bi_2Te_{2.7}Se_{0.3}$, which increases from $ZT = 0.85$ to $ZT = 1.04$ at 400 K in the direction perpendicular to pressing, can be achieved by hot forging samples prepared by ball milling.[155] Hu *et al.* report hot forged *n*-type $Bi_{1.95}Sb_{0.05}Te_{2.3}Se_{0.7}$ with $ZT \approx 1.3$ at 450 K due to the presence of multiscale microstructures.[156] For $Bi_{1.95}Sb_{0.05}Te_{2.3}Se_{0.7}$, five successive hot-forging steps were used to increase the Lotgering factor *F*, to 0.79, as well as to introduce multiscale structural defects, which resulted in a lattice thermal conductivity as low as $\kappa_L = 0.31$ W m^{-1} K^{-1} at 405 K.[156] Hot forging of $Ca_3Co_4O_9$ enhances the electrical conductivity without lowering the Seebeck

coefficient, and therefore improves the power factor, which reaches a value of $S^2\sigma$ = 0.8 mW mK^{-2} at 1,073 K.[157] In $Bi_{0.875}Ba_{0.125}CuSeO$, hot forging increases the ratio σ/κ_{total} in the out-of-plane direction and leads to an increase in the figure of merit from *ZT* ~1.1 to *ZT* ~1.4 at 923 K after three hot-forging steps.[151]

1.3.4 Other consolidation approaches

The vast majority of commercial thermoelectric modules are based on Bi_2Te_3 alloys, for which aligned polycrystalline ingots and single crystals are grown from a melt, for instance by zone melting.[158] The *n*- and *p*-type legs for the modules are produced by cutting from large ingots, without any need for powder consolidation. Due to the limitations of HP or SPS for large-scale production, hot extrusion, which entails hot pressing the thermoelectric material through a draw die, is another method used commercially to produce Bi_2Te_3 thermoelements. Hot extrusion introduces texture, and more importantly, improves the mechanical properties of Bi_2Te_3.[158] A study by Ivanova *et al*.[159] has shown that hot extrusion of *p*-type $Bi_{0.6}Sb_{1.4}Te_3$ produces materials with figures of merit comparable to those of Czochralski-grown single crystals. Hot extrusion has also been applied to produce *n*-type PbTe rods of up to 2 kg, which are less brittle than conventionally-processed materials and exhibit a thermoelectric performance comparable to those of Bridgman-grown materials.[160]

High-pressure torsion, in which the sample undergoes severe plastic deformation when torsional strain is applied under pressure between two anvils,[161] has also been exploited in an effort to improve the figure of merit. High-pressure torsion reduces the grain size and produces a high concentration of deformation-induced defects, lowering the lattice thermal conductivity. For example, skutterudites with figures of merit approaching *ZT* = 2 have been produced using this method.[162]

1.4 Property measurements

Prior to measurements of physical properties, it is good practice to determine the density of the consolidated materials and to compare this with the theoretical (crystallographic) density, determined by the crystal structure of the material. Property measurements should be carried out on samples with densities as close as possible to the theoretical density. Figures of merit for porous samples (non fully densified) often differ markedly from those of well-consolidated samples, as porosity increases the electrical resistivity and reduces the thermal conductivity.[163,164] After consolidation, it is also advisable to assess the sample purity and homogeneity using X-ray diffraction, SEM and EDAX, as the presence of impurities introduced during the consolidation process (Section 1.3) may affect the charge-carrier concentration of the main phase. Similarly, sample inhomogeneities could result in errors in the figure of merit if the contributing properties were to be measured on different samples;[165] it is preferable to measure all properties on the same ingot wherever possible. When property measurements are carried out along different directions of the consolidated ingots, consideration must be given to the texture of the samples. For materials with anisotropic properties, measurement of the electrical and thermal conductivities along different directions could result in an overestimation of the figure of merit by up to 60%.[166]

Determination of the figure of merit usually involves measuring the electrical conductivity, σ, Seebeck coefficient, S, and thermal conductivity, κ, although direct measurement of ZT is also possible (Section 1.4.5).[167] For the complete characterisation of thermoelectric materials, Hall coefficient measurements (Section 1.4.3), which provide information on charge-carrier concentration and mobility, are also desirable. In the following sections, the principles on which these measurements are based will be discussed, together their limitations, sources of error and important considerations for the reliable determination of thermoelectric properties. A discussion of available standards for these measurements can be found in reference 168.

1.4.1 Electrical conductivity and resistivity

The electrical conductivity, σ, is an intrinsic property of matter which quantifies how well a substance conducts an electrical current. The electrical conductivity depends on the number of carriers, n, and their mobility, μ:

$$\sigma = ne\mu \qquad (1.13)$$

where e is the charge of the carrier. The electrical conductivity is inversely proportional to the electrical resistivity, ρ:

$$\rho = \frac{1}{\sigma} \qquad (1.14)$$

The electrical resistivity depends on the resistance to flow of an electrical current, R, and the dimensions of the material:

$$\rho = R\frac{A}{L} \qquad (1.15)$$

where R is given in ohms (Ω), and L and A are the length and the cross-sectional area of the sample respectively. The SI unit of electrical resistivity is Ω m, while the electrical conductivity is given in S m^{-1} (or Ω^{-1} m^{-1}). For intrinsic (non-doped) broadband semiconductors, electrical conduction requires thermal excitation of charge carriers across a bandgap, and therefore the electrical conductivity may be given by:

$$\sigma = \sigma_0 e^{-E_g/2k_BT} \qquad (1.16)$$

where σ_0 is a proportionality constant, E_g is the bandgap energy, k_B is the Boltzmann constant, and T is the absolute temperature. The electrical conductivity of intrinsic semiconductors increases with temperature. However, thermoelectric materials are heavily doped and often behave as degenerate semiconductors. In a degenerate semiconductor the level of doping is sufficiently high that the Fermi level, E_F, is located in either the valence or

conduction band. This causes the material to behave like a metal, with the electrical conductivity exhibiting a metal-like decrease with increasing temperature.

In materials with narrow bands, where the charge carriers behave as localised particles (small polarons), electronic conduction may occur by hopping. In this case, the electrical conductivity may be given by:[169]

$$\sigma = \frac{\sigma_0}{T} e^{-W/k_B T} \qquad (1.17)$$

where W is the activation energy for hopping. A variable-range hopping (VHR) behaviour may be found in materials which are disordered, and where the charge carriers are hopping between localized states. This will result in the following temperature dependence for the electrical conductivity:[170]

$$\sigma = \sigma_0 \, exp\left(\frac{T_0}{T}\right)^{1/j+1} \qquad (1.18)$$

where T_0 denotes the hopping energy and j refers to the dimensionality of VRH conduction.

[Figure 1.12 near here]

The most straightforward approach to measure electrical resistivity is a two-probe method (Figure 1.12(a)), in which two measuring probes are connected to the sample, and the voltage drop across the sample is measured when a current passes. According to Ohm's law, the resistance of the sample will be given by:

$$R = \frac{V}{I} \qquad (1.19)$$

where V and I are the voltage and electrical current respectively, and therefore the resistivity can be determined using Eq. (1.15). However, two-probe measurements include contact resistances, as well as contributions from the resistance of the wires and from the measuring equipment, which increase the measured resistance above its true (intrinsic) value. While the two-probe technique could be used for samples with large resistivities, it is unsuitable for

thermoelectric materials, which by their very nature, have low electrical resistivities. For accurate measurement of such materials, a four-probe method should be used (Figure 1.12(b)).

In the four-probe method, the electrical current flows between two contacts at the ends of the sample under test, and the voltage drop is measured between two inner contacts. This arrangement eliminates the contributions described above. However, to ensure that there is a uniform current distribution between the two inner voltage contacts, these must be placed by at least a distance equivalent to one width of the sample from the ends.[171] Poor thermal contact between the sample and the thermocouple can lead to inaccurate temperature readings, which can introduce errors into the measurements.[165] Another potentially important source of error in the case of thermoelectric materials is the presence of a temperature difference across the sample, which can arise due to existing thermal gradients, Joule heating or the Peltier effect. If the temperature at each of the two inner contact points is different, an additional Seebeck voltage will be generated, and given that thermoelectric materials necessarily exhibit reasonably large Seebeck coefficients, this could be appreciable. The total voltage measured across the sample is the sum of the resistive voltage, IR, and the Seebeck voltage, $S\Delta T$:

$$V_{\text{total}} = IR + S\Delta T \qquad (1.20)$$

This problem can be minimised by determining the average voltage when the same current is passed in opposite directions (I^+ and I^-), as this will remove the Seebeck contribution. The average voltage will be given by:[172]

$$V = \frac{[V(I^+)+S\Delta T]-[V(I^-)+S\Delta T]}{2} \qquad (1.21)$$

where I^+ is the positive current and I^- the negative current. The quality of the electrical contacts, which should be ohmic, can be tested with an *I*-*V* sweep. This requires measurements of current and voltages over a range of currents; a plot of *V* vs. *I* will be linear

if the contacts are ohmic. The values of resistivity determined by the four-probe method are sensitive to errors in the measurement of the dimensions of the sample. This can introduce an error of up to 10% in the measured resistivity.[173]

An alternative approach to the four-probe method, which is less sensitive to errors in geometric factors, is the van der Pauw method (Figure 1.12(c)).[174] This allows measurements to be made on thin samples of arbitrary shapes, providing they have a uniform thickness. Four contacts (A, B, C and D) are placed on the edges of the sample, and the resistances $R_{AB,CD}$ and $R_{BC,DA}$ are then defined as:

$$R_{AB,CD} = \frac{V_D - V_C}{I_{A-B}} \text{ and } R_{BC,DA} = \frac{V_A - V_D}{I_{B-C}} \qquad (1.22)$$

where V_D-V_C is the voltage difference between D and C, $I_{A\text{-}B}$ is the current between A and B, etc. The electrical resistivity of the material is given by:

$$\rho = \frac{\pi d}{\ln 2} \frac{R_{AB,CD} + R_{BC,DA}}{2} f \qquad (1.23)$$

where d is the thickness of the sample, and f is a function dependent on $R_{AB,CD}$ and $R_{BC,DA}$, details of which can be found in reference 175.

For measurements at low temperatures, electrical contacts can be made using electrically-conductive epoxies or solders, while at high temperatures, contacts are made by pressing probes directly onto the surface of the sample. Tritt has provided a useful summary of contact techniques.[172] The vast majority of measurements reported for thermoelectric materials are carried out using commercial instruments (Quantum Design Physical Properties Measurement System (PPMS) for low temperatures, and Linseis LSR series or Ulvac ZEM series for measurements above room temperature), all of which use a 4-probe method. There are also reports of custom-made apparatuses which can accommodate a variety of sample sizes and geometries and often combine resistivity measurements with those of other properties.[176,177]

1.4.2 Seebeck coefficient

The Seebeck effect,[178] which lies at the heart of thermoelectric power generation, can be described by considering a thermocouple, formed by two dissimilar materials, A and B, joined at two junctions, labelled 1 and 2 (Figure 1.13). If junctions 1 and 2 are at different temperatures, T_1 and T_2, an electrical potential will develop between points 3 and 4. The voltage difference (dV) between points 3 and 4 will be directly proportional to the temperature difference (dT), with the coefficient of proportionality being the Seebeck coefficient, S:

[Figure 1.13 near here]

$$dV = S_{AB}dT \qquad (1.24)$$

where S_{AB} is the relative Seebeck coefficient ($S_{AB} = S_A - S_B$) between materials A and B. Although the SI units of the Seebeck coefficient are V K^{-1}, values are usually presented in the more convenient units of μV K^{-1}. In order to determine the absolute Seebeck coefficient for a given material, A, the Seebeck coefficient for the reference material, B, must be known over the temperature range of the measurements. Usually the reference materials (i.e. the measurement wires) used for Seebeck coefficient measurements are metals with small values of the Seebeck coefficient. For example, platinum exhibits an absolute Seebeck coefficient at room temperature of only -5 μV K^{-1}.[179] Representative values of the Seebeck coefficient for some typical metals and semiconductors are shown in Table 1.7.[180,181]

From a physical point of view, the Seebeck coefficient is the heat per carrier over temperature or the entropy per carrier, and can be expressed as:

$$S = \frac{c}{q} \qquad (1.25)$$

where c is the heat capacity (i.e. heat/temperature) and q is the charge of the carrier.[182] Therefore the Seebeck coefficient provides information about the sign of the charge carriers. Materials in which electrical conduction is dominated by electrons have a negative Seebeck

coefficient and when conduction is dominated by holes, the Seebeck coefficient is positive. If both types of charge carrier are present, the Seebeck coefficient is given by their average, weighted by their electrical conductivities:[178]

$$S = \frac{S_n \sigma_n + S_p \sigma_p}{\sigma_n + \sigma_p} \qquad (1.26)$$

where σ_n and σ_p are the electrical conductivities of electrons and holes, respectively. In intrinsic semiconductors, both types of charge carriers contribute to the electrical conduction, and as S_n and S_p have opposite signs, the total Seebeck coefficient will be reduced. Therefore, in order to maximise the Seebeck coefficient, it is necessary to minimise the contribution of the minority charge carriers.

Since the Seebeck coefficient is related to the heat transported per carrier, if we consider a metal as a degenerate electron gas, with $E_F >> k_B T$, the Seebeck coefficient will be given by:[182]

$$S \sim \left(\frac{k_B}{e}\right)\frac{k_B T}{E_F} \qquad (1.27)$$

where E_F is the Fermi energy, k_B the Boltzmann constant and $k_B/e \approx 87$ μV K^{-1} is the Seebeck coefficient of a classical electron gas. Therefore, the Seebeck coefficient of a metal will be much less than 87 μV K^{-1} (as $E_F >> k_B T$), and will increase with increasing temperature. Typically, the absolute value of the Seebeck coefficient of a metal ($|S|$) is between 1 and 10 μV K^{-1}.

For an extrinsic semiconductor with one type of charge carrier the following expression has been derived:[182]

$$S \sim \frac{k_B}{e}\frac{E_g}{2k_B T} \qquad (1.28)$$

and therefore semiconductors exhibit Seebeck coefficients larger than 87 μV K^{-1} (since $E_g >> k_B T$ to avoid intrinsic conduction) that increase with decreasing temperature. It should be

noted however that the temperature dependence of the Seebeck coefficient can show greater complexity; models for semiconductors containing more than one type of carrier or for conduction through hopping have been discussed by Chaikin.[182] For instance, when hopping conduction occurs, the Seebeck coefficient is given by the Heikes formula:[183]

$$S = \frac{k_B}{e} \, ln\left[\frac{1-x}{x}\right] \qquad (1.30)$$

where x and 1-x represent the content of the lower (M^{n+}) and higher ($M^{(n+1)+}$) oxidation states present in the material. This expression is widely used to interpret Seebeck data for transition metal oxides.[184]

In semiconductors, the onset of bipolar conduction occurs when the temperature is high enough for thermal excitation of electrons across the band gap to take place, and is characterised by a change in the temperature dependence of the Seebeck coefficient. The maximum absolute value of the Seebeck coefficient, $|S_{max}|$, can be related to the band gap by the following expression:[185]

$$E_g \approx 2e|S_{max}|T_{max} \qquad (1.29)$$

where T_{max} is the temperature at which $|S_{max}|$ is reached. While Eq. (1.29) provides a convenient way to estimate the bandgap, significant deviations from the true value of the bandgap can occur, particularly when $|S_{max}| < 150$ μV/K^{-1}.[186]

There are two approaches to measurement of the Seebeck coefficient: the integral and the differential methods.[187] In the integral method (or large ΔT), one end of the sample under test is maintained at a constant temperature, T_1, while the temperature at the other end, T_2, is varied through a temperature range, $T_2 = T_1 + \Delta T$. In the differential method, which is the more commonly-used approach in both commercial and custom-made equipment, a small temperature gradient ($\Delta T = T_2 - T_1$) is applied at the average temperature of interest, $T_{ave} = (T_1 + T_2)/2$, (where $T_{ave} >> \Delta T$) and the Seebeck coefficient at T_{ave} is obtained as $V/\Delta T$. This

procedure is repeated at different average temperatures, in order to determine the Seebeck coefficient as a function of temperature.

Measurements using the differential method can be carried out under steady-, quasi-steady- and transient-state conditions, all of which have been discussed in detail by Martin *et al*.[187] A brief description of the steady-state differential method follows, in order to highlight potential sources of error in Seebeck coefficient measurements. In the steady-state differential method, several (V, ΔT) data points are collected, while ensuring the sample temperature is stabilised before each data point collection. The Seebeck coefficient at T_{ave} is calculated as the slope of a V vs. ΔT plot. This eliminates offset errors (as in practice the line of the best fit will not pass along the origin, ($V = 0$, $\Delta T = 0$), due to thermocouple inhomogeneities and nonequilibrium contact interfaces. The disadvantage of the steady-state method is that equilibration of the sample before each (V, ΔT) data point measurement is time consuming, hence quasi-steady-state conditions are often used. A recent study has shown that there is little difference between the steady-state and the quasi-steady-state methods if thermal and electrical contacts are good.[188,189] If possible, it is advisable to measure (V, ΔT) data points for both an increasing and decreasing ΔT. Any hysteresis in the data may be an indicator of poor thermal contact.[165]

[Figure 1.14 near here]

Seebeck coefficient measurements can be carried out using 2-probe or 4-probe arrangements (Figure 1.14). These two arrangements have arisen in part from the desire to combine Seebeck coefficient measurements with determination of either thermal or electrical conductivity. In the 2-probe arrangement, V and ΔT are measured on the two probes located at either end of the sample (Figure 1.15(a)). In this arrangement, the thermocouple and voltage wires are not in direct contact with the sample, and are instead embedded in metal blocks at either end. Good thermal and electrical contact with the sample is therefore needed.

In the 4-probe arrangement, which is required for simultaneous measurements of electrical conductivity and Seebeck coefficient, the two end probes are used to create a temperature gradient, while V and ΔT are measured at two points on the sample separated from the two end probes (Figure 1.14(b)). In this arrangement, the two probes used for the V and ΔT measurements are in direct contact with the sample. There has been very little comparison of the results obtained using these two arrangements. According to recent work,[188,189] the difference between Seebeck coefficient values measured with a 2-probe arrangement and those measured with a 4-probe arrangement increases with increasing temperatures. Due to cold finger effects, the 4-probe contact geometry overestimates the Seebeck coefficient, while a 2-probe geometry underestimates it. Round-robin studies, in which the same sample is measured in several laboratories world-wide, indicate that a variation of ±5% in the measured Seebeck coefficient will occur at room temperature, and that this variation increases with increasing temperature.[173,190] For high-temperature Seebeck measurements, commercial instruments (Linseis LSR or Ulvac ZEM series), which perform simultaneous Seebeck coefficient and electrical conductivity measurements using a 4-probe arrangement, are widely used. An overview of custom-made apparatus for Seebeck measurements can be found in reference 187.

1.4.3 Hall-effect measurements

Hall-effect measurements enable determination of the charge carrier type, together with the carrier density and mobility. Although this information is not required to calculate the figure-of-merit, ZT, it is often important in order to gain a good understanding of a thermoelectric material. The power factor usually reaches an optimal value at charge-carrier concentrations of around 10^{19} cm^{-3}, and therefore the optimisation of figure of merit requires doping of thermoelectric materials. The physical basis of the Hall effect is as follows:[191,192] when an

electrical current flows through a material and a magnetic field is applied perpendicular to the current, a voltage, known as the Hall voltage, is produced in the direction perpendicular to both the electric and magnetic fields. This is illustrated in Figure 1.15, where an electrical field, applied along the *x* direction, results in a current I_x. When a magnetic field, B_z, is applied along the *z* direction, charge carriers are deflected along *y*, producing a Hall voltage, V_H. As shown in Figure 1.15, electrons and holes are deflected in opposite directions, hence the sign of the Hall voltage provides information on the identity of the charge carrier. The magnitude of the Hall voltage, which depends on I_x, B_z and the thickness of the sample, *d*, is given by the expression:

$$V_H = \frac{R_H I_x B_z}{d} \qquad (1.31)$$

where the Hall coefficient, R_H, is related to the concentration of charge carriers, *n*, by:

$$R_H = \frac{1}{ne} \qquad (1.32)$$

[Figure 1.15 near here]

The Hall coefficient is negative for conduction by electrons, and positive when the charge carriers are holes. The charge-carrier mobility, μ, may be determined from:

$$\mu = \frac{R_H}{\rho} \qquad (1.33)$$

It should be noted however that the equations above are based on the free electron model, and hence for materials with complex band structures, the mobility and charge-carrier concentration, determined from Hall-effect measurements, could differ significantly from the true values of charge-carrier concentration and mobility.[165] Nonetheless, Hall measurements provide a useful comparison of compositionally-induced changes in charge-carrier densities on chemical substitution within a given material system.

The most common arrangement for Hall-coefficient measurements is a van der Pauw geometry (Figure 1.12(c)), where the same four contacts are used for resistivity and for Hall-coefficient measurements.[174,193] The problems associated with measurements of the Hall effect are similar to those found for the measurement of electrical resistivity (Section 1.4.1). Errors will arise if the contacts are non ohmic, or if the contacts are displaced from their correct positions.[194] As the Hall voltage is often very small, other contributions, such as the Seebeck voltage arising from a temperature gradient in the sample, can be significant. Hall measurements can be performed in DC mode, and by repeating the measurement with the magnetic field reversed, most offset voltages are removed (with the exception of a small contribution from the Ettinghausen effect).[172] Many thermoelectric materials have large charge-carrier mobilities, which can be measured using a DC Hall-effect technique, but for measurements on materials with low mobilities, an AC method is more suitable.[195]

1.4.4 Thermal conductivity

Thermal conductivity is a transport property which describes the movement of heat from high-temperature to low-temperature regions. The thermal conductivity of a material, κ, is defined as the coefficient of proportionality between the heat flux and the temperature gradient across the material. For a material with a temperature gradient along the x direction, the following expression can be written:

$$J_x(Q) = -\kappa \frac{dT}{dx} \qquad (1.34)$$

where the heat flux, $J_x(Q)$, is the amount of heat that flows per unit time per unit area (measured in W m^{-2}), κ is the thermal conductivity and dT/dx is the temperature gradient along the x direction. The thermal conductivity of a material determines whether it is a thermal conductor (large κ) or a thermal insulator (low κ). Typical values of thermal

conductivities are shown in Table 1.8.[196,197] The unit generally used for thermal conductivity is W m^{-1} K^{-1}.

Heat in solids is transported principally by quantized vibrations, termed phonons, and by electrons. The total thermal conductivity can be considered to be the sum of two contributions:

$$\kappa = \kappa_L + \kappa_E \qquad (1.35)$$

where κ_L is the lattice thermal conductivity, due to phonon transport, and κ_E is the electronic thermal conductivity. The electronic thermal conductivity, κ_E, and the electrical conductivity, σ, are related through the Wiedemann–Franz law:

$$\kappa_E = L_0 \sigma T \qquad (1.36)$$

where L_0 is the Lorenz number. For most metals this takes a value of $L_0 = 2.44 \times 10^{-8}$ W Ω K^{-2}.

A high thermoelectric figure of merit requires a material to possess a low total thermal conductivity and a high electrical conductivity. Since σ and κ_E are directly related, a commonly used approach to improve the figure of merit is to reduce κ_L. The value of κ_L is normally estimated using equations (1.35) and (1.36). Although some thermoelectric materials have a Lorenz number close to the degenerate limit of $L_0 = 2.44 \times 10^{-8}$ W Ω K^{-2}, this is not always the case, and an incorrect value of the Lorenz number can result in erroneous values of κ_L. A straightforward approach to estimate the value of L_0, from the Seebeck coefficient, is through the expression:[198]

$$L_0 = 1.5 + exp\left(-\frac{|S|}{116}\right) \qquad (1.37)$$

where the units of L_0 are 10^{-8} W Ω K^{-2} and those of S are μV K^{-1}. The estimated error in the Lorenz number determined using Eq. (1.37) is below 20% for the most common band

structures (parabolic or non-parabolic) and scattering mechanisms (acoustic phonon, ionized impurities, polar and alloy scattering), found in thermoelectric materials.[198]

When compared to measurement of electrical conductivity or Seebeck coefficient, reliable measurement of thermal conductivity is more challenging, as it is difficult to avoid heat losses completely. As discussed by Goldsmid,[199] radiative heat transfer will still occur even when a material is placed under the high vacuum necessary to prevent heat transfer by conduction and convection.

The most commonly-used technique for the determination of the thermal conductivity of thermoelectric materials is the laser-flash method that will be discussed here. However, it should be noted that there are other methods available (Table 1.9), which can be classified into the two broad categories of steady-state and transient techniques. In the steady-state method, the thermal conductivity is determined using a temperature difference which remains unchanged with time, while transient techniques measure a time-dependent energy dissipation process.[200] These methods, which are beyond the scope of this chapter, have been reviewed in detail in references 200 and 201.

[Table 1.9 near here]

[Figure 1.16 near here]

The laser-flash method measures the thermal diffusivity, D, which is related to the thermal conductivity by:

$$\kappa = D\, d\, C_p \qquad (1.38)$$

where d is the sample density, and C_p is the heat capacity at constant pressure. Therefore, in order to determine the thermal conductivity from diffusivity data, additional measurements of both density and heat capacity are required. In the laser-flash method, one face of the sample is irradiated with a short pulse of heat (generated with a xenon flash lamp or a laser), while an infra-red (IR) detector monitors the temperature on the reverse face (Figure 1.16). As this

method assumes only an axial flow of heat, with no lateral heat losses, the sample is required to be in the form of a thin disk, with a large cross sectional area relative to its thickness. To maximise the absorption of radiation and the emissivity, and hence the signal received by the IR detector, the top and bottom sample faces are often coated with a thin layer of graphite. Careful sample preparation is essential, as thick graphite coatings or poor adhesion of the graphite to the sample can introduce significant errors.[165] The top and bottom faces of the sample must be parallel, in order to minimize the error in sample thickness. The thermal diffusivity of the sample is related to the time required to reach half of the maximum temperature rise, $t_{1/2}$, according to:[202]

$$D = \frac{1.38\, l^2}{\pi^2 t_{1/2}} \qquad (1.39)$$

where *l* is the sample thickness. Commercial laser-flash instruments, which normally perform a least-squares fit to the transient curve to determine the diffusivity, can also apply corrections (due to Cowan,[203,]and to Clark and Taylor[204]) that take into account heat losses through the top and bottom faces and the sides of the sample. The scatter in thermal diffusivity measurements between laboratories worldwide has been found to be of the order of ±8 for Bi_2Te_3[205] and of ± 9.5% for $Co_{0.97}Ni_{0.03}Sb_3$,[190] although smaller variations of ±1.9% at 323 K and ±3.7% at 773 K were reported from a round-robin study on an *n*-type half-Heusler material, in which greater care was taken with the determination of sample thickness.[206]

In order to extract thermal conductivity values from measurements made by the laser-flash method, heat capacity measurements are required. Although commercial laser-flash instruments can measure heat capacities by a comparative method, using a reference material of known heat capacity, the accuracy of these measurements can be low. A Quantum Design Physical Properties Measurement System (PPMS) with the heat capacity option can be used for heat capacity measurements at low temperatures, and Differential Scanning Calorimetry

(DSC) is frequently used to determine heat capacities above room temperature. DSC heat capacity measurements should follow the ASTM standard E1269,[207] which requires three separate scans: a baseline (empty pan), a sapphire standard and the sample. It is also advisable to remeasure the baseline after completing measurement of the sample under test, as changes in the baseline could affect the determination of heat capacity. Experienced DSC operators can achieve variations as low as *ca*. ±4% in heat capacity measurements, although often the scatter is significantly higher.[205] For measurements above the Debye temperature of the material, a quality check of the heat-capacity data can be readily carried out by comparing the measurements with the calculated Dulong-Petit value. According to the Dulong-Petit law, the specific heat under constant volume, C_v, is 3R per mole of atoms. For a material with a molar mass M containing n atoms per formula unit, the Dulong-Petit heat capacity, C_v^{DP}, in J g^{-1} K^{-1} can be expressed as:

$$C_v^{DP} = \frac{n\,3R}{M} \qquad (1.40)$$

The Dulong-Petit heat capacity is related to C_p by: [205]

$$C_p = C_v^{DP} + \frac{\alpha^2 T}{\beta_T d} \qquad (1.41)$$

where α is the coefficient of thermal expansion, β_T the isothermal compressibility and d the density. While C_v^{DP} is constant with temperature, C_p should be slightly higher and increase with increasing temperature. A round-robin study suggests that the experimental heat capacity should be expected to be within ±5% of the Dulong-Petit value, for high-quality measurements.[205] For materials with Debye temperatures significantly lower than the measurement temperatures, it may be a reasonable approximation to calculate the thermal conductivity using the Dulong–Petit value when DSC measurements are not available, or when heat-capacity measurements appear to be unreliable.[206]

Density measurements are also needed to calculate the thermal conductivity. For samples with a regular shape, the geometric density, calculated using the sample volume and mass can

be used. Alternatively, the Archimedes method, in which the sample is immersed in a liquid, can be employed.[208] For the calculation of the thermal conductivity, the density is usually treated as temperature independent. Toberer has considered the effect of correcting the density, heat capacity and diffusivity measurements for thermal expansion, and has shown that, in the case of $Ba_8Ga_{16}Ge_{30}$, the variation in thermal conductivity would be 1.2% at high temperature.[62] This value is significantly smaller than the uncertainty in thermal conductivity values. Taking into account error propagation from the individual measurements of diffusivity, density and heat capacity, the uncertainty in the derived thermal conductivity values has been estimated to range between ± 6.3 and 10.4 %, with the uncertainty increasing with increasing temperature.[206]

1.4.5 **Direct measurement of *ZT***

The measurement uncertainties of commercial instruments for the individual physical properties that contribute to the figure of merit are, according to Wei *et al.*,[209] ±3% for electrical conductivity, ±4% for Seebeck coefficient, ±1% for density, ±3% for thermal diffusivity and ±5% for heat capacity. Round-robin studies have revealed significant variations in measured values for individual properties.[171,190,205,206] The combination of these individual uncertainties will result in a significant error in the figure of merit, which has been estimated as ±11.5 to ±16.4% for an *n*-type half-Heusler material,[206] or ±11.7 to ±20.9% for Bi_2Te_3,[205] depending on the temperature. Given uncertainties in the individual measurements which contribute to a large uncertainty in the figure of merit, methods for the direct measurement of *ZT* are clearly attractive.

In the Harman method, *ZT* is determined by measuring the voltage across the sample under isothermal conditions (i.e. in the absence of a temperature gradient), and under adiabatic conditions.[167] To reach adiabatic conditions, an electrical current is passed through the

sample until a steady state, where the heat transported due to the Peltier effect along one direction of the sample is equal to the heat transported in the opposite direction by thermal conduction, is reached. Neglecting Joule heating and heat loses, it can be shown that *ZT* is given by:[171]

$$ZT = \frac{V_a}{V_i} - 1 \qquad (1.42)$$

where V_a is the adiabatic voltage, and V_i is the isothermal voltage. A theoretical treatment to account for heat losses and Joule heating has also been discussed by Nolas *et al.*[171] In order to apply the Harman technique, contact effects, sample resistance, and sample heating from the contacts must be negligible, and the sample typically needs to exhibit a figure of merit, $ZT \geq 0.1$ (to produce the required large difference between V_a and V_i).[201] Implementations of the technique that enable the determination of the electrical conductivity, thermal conductivity and Seebeck coefficient, together with *Z*, have been described.[171,201,210] Parasitic heat-exchange effects between the sample and its environment are critical for measurement accuracy: if parasitic thermal effects are not taken into account, measured values of *Z* determined by the Harman method could vary by up to 50% when the sample dimensions[211] or the electrical contacts are changed.[212] A two-sample system calibration, which enables the evaluation of thermal losses during measurements, has been developed.[210] The accuracy of measurements using the two-sample system calibration has been estimated to be better than 5% for the figures of merit at temperatures up to 700 K.[213] More extensive testing of this approach, using a wide range of materials, is needed.

Impedance spectroscopy, a technique widely used in fields such as photovoltaics, fuel cells and supercapacitors, can also be exploited for the characterisation of both thermoelectric materials and complete devices.[214] This technique is based on the application of a small sinusoidally-varying voltage to the material or device under investigation and the analysis of the response current, which may be in or out of phase with respect to the voltage, as a

function of frequency.[215] The impedance is given by the AC voltage divided by the AC current. In complex number notation, the impedance, Z^*, can be expressed as: $Z' = |Z^*|\cos\theta$ and $Z'' = |Z^*|\sin\theta$, where θ is the phase between voltage and current, and Z' and Z'' are the real and the imaginary parts of the impedance, respectively. Data are conveniently presented in a Nyquist plot of Z'' as a function of Z'. Equivalent circuits that enable the analysis of the Nyquist plots for thermoelectric materials are available;[216] the Seebeck coefficient, electrical resistivity, thermal diffusivity, specific heat, thermal conductivity and figure of merit at a given temperature can all be extracted from these data. An experimental setup that enables measurements between 323 and 523 K has been recently described.[217,218] This technique is also useful as a rapid test to evaluate the quality of thermoelectric module fabrication.[45]

1.5 Conclusions

The methods that are most commonly used for the synthesis, consolidation and measurements of thermoelectric materials have been described. Common problems encountered with each technique, together with their advantages and disadvantages, have been discussed. Much of the research in thermoelectric materials is driven by efforts to increase the maximum figure of merit, *ZT*, which is related to the efficiency of thermoelectric energy recovery. However, the efficiency of a thermoelectric device (Eq. (1.1)) depends on the average figure of merit, $(ZT)_{ave}$, across the temperature range of operation. For this reason, increasing $(ZT)_{ave}$ (rather than the maximum figure of merit) has a more marked impact on the efficiency of energy recovery. This is particularly important for materials that show a sudden increase in *ZT*, for instance, due to a phase transition. Researchers in this field should therefore consider the $(ZT)_{ave}$ of their materials, as well as the maximum value.

To ensure that meaningful results in materials development are obtained, careful characterisation of the materials is essential. This extends from the assessment of sample

purity and homogeneity following synthesis and consolidation, given that the presence of secondary phases could affect the charge carrier concentration, to the measurements, which should be of the highest quality, with errors as low as possible. The reproducibility of results should evaluated, and instruments should be regularly checked with standards, to ensure that, for example, thermocouple degradation has not occurred. The thermal stability of thermoelectric materials across the temperature range of operation should also be considered. Oxidation or volatilisation of certain elements can occur at elevated temperatures. For instance, the composition of skutterudites and sulfides may change on heating due to volatilisation of antimony and sulfur, respectively. Thermogravimetric analysis (TGA) of materials under different atmospheres (e.g. nitrogen, air) can provide valuable information about stability. Compositional changes when a thermoelectric device is exposed to elevated temperatures can result in materials degradation and hence a fall-off in performance. Repeated measurements of the properties, to ensure thermoelectric performance does not degrade following the initial measurement, should be performed.

The discovery and thermoelectric characterisation of a promising new thermoelectric material is only the first step. Incorporation of a new material into a thermoelectric device is technologically challenging. In a device, the *n*- and *p*-type legs are interconnected by soldering to a metal strip, and contact layers, with low contact resistances, are required. Contact layers suitable for existing materials such as Bi_2Te_3, may not be transferable to a newly discovered material. Reaction of the thermoelectric materials with the contact layers and/or solders can lead to degradation or failure of the device. Matching the coefficients of thermal expansion of the different device components is also essential, to avoid stress and possible fracture of the device during operation. To achieve progress in the practical implementation of thermoelectric technology, successful research efforts resulting in the

discovery of a new thermoelectric material must be followed by work that addresses the device level challenges.

Figure Captions

Figure 1.1	Schematic representation of a thermoelectric couple, composed of two semiconducting materials; one *p*-type and other *n*-type, which are joined by a metal strip (black bar), to make a junction. Power generation occurs when one end of the junction is heated.
Figure 1.2	Schematic representation of the solid-state reaction between particles of the elements A and B, in contact at a common surface, to form a product AB.
Figure 1.3	The evacuated sealed-tube method, which involves (a) evacuating a glass ampoule which contains the powdered sample, (b) sealing the ampoule using a gas-oxygen torch, and (c) heating the sealed ampoule in a furnace.
Figure 1.4	Types of ball mills: (a) planetary ball mill; (b) vibration (shaker) mill and (c) attrition mill used in the mechanosynthesis of thermoelectric materials. Adapted from reference 25 with permission from The Royal Society of Chemistry.
Figure 1.5	Powder X-ray diffraction pattern of (a) the initial product from ball-milling a mixture of stoichiometry Cu_5FeS_4 and (b) after hot-pressing the initially-formed product to produce Cu_5FeS_4. Unreacted iron in (a) is marked with a star.
Figure 1.6	Methods for the growth of large single crystals: (a) Czochralski method; (b) Bridgman method.
Figure 1.7	A schematic diagram of a Teflon-lined Stainless-steel autoclave, composed of: (a) stainless-steel lid; (b) pressure plate; (c) corrosion

	and rupture discs; (d) stainless-steel body; (e) Teflon liner; (f) spring, (g) solvent; (h) solid reagents.
Figure 1.8	Schematic diagram illustrating colloidal synthesis. In the “heat-up” method, heating occurs after adding all reagents. In the “hot-injection” method, the final reagent is added once the reaction mixture in the round-bottom flask is hot.
Figure 1.9	Schematic representation of the three stages of sintering, together with the corresponding densification curve.
Figure 1.10	Schematic diagrams of (a) a hot-press apparatus and (b) a spark plasma sintering (SPS) apparatus, which differ in the method used to heat the sample.
Figure 1.11	Schematic representation of the hot forging process, which entails using a die larger than the ingot: (a) a consolidated ingot (pale blue) is placed inside a die of a larger diameter; (b) pressure and temperature are applied; resulting in (c) the formation of a consolidated ingot of a larger diameter and with a higher degree of preferred orientation.
Figure 1.12	The three common techniques for the measurement of the electrical resistivity of a material: (a) two-probe method, (b) four-probe method, and (c) van der Pauw method.
Figure 1.13	Schematic diagram of a thermocouple formed by two dissimilar materials A and B, joined at the junctions 1 and 2.
Figure 1.14	Probe arrangements for Seebeck coefficient measurements: (a) 2-probe, and (b) 4-probe. The heaters to create a temperature gradient

	are shown in red and blue and the thermocouples to measure V and ΔT are shown as black lines.
Figure 1.15	Schematic diagram of the Hall effect. Electrons and/or holes in the current, I_x, are deflected by the magnetic field B_z. This generates the Hall voltage, V_H.
Figure 1.16	Schematic diagram of a laser-flash instrument for the measurement of thermal diffusivity.

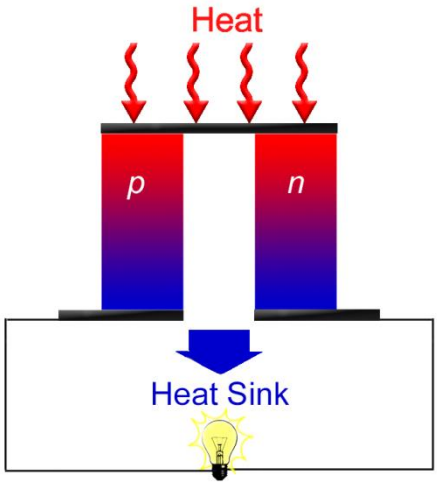

Figure 1.1

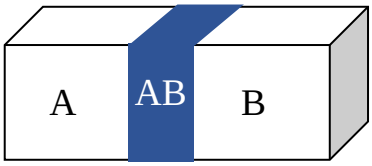

Figure 1.2

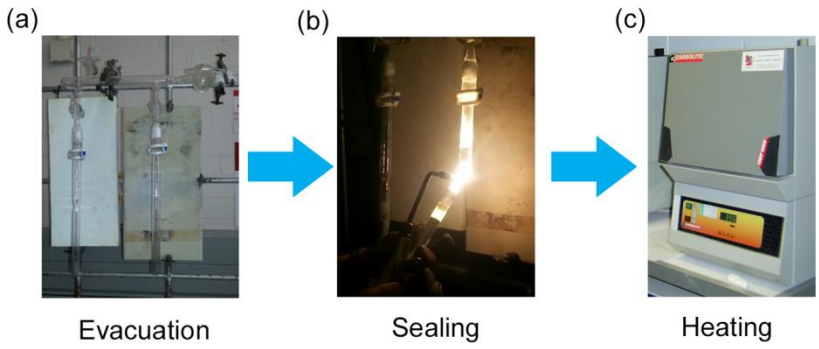

Figure 1.3

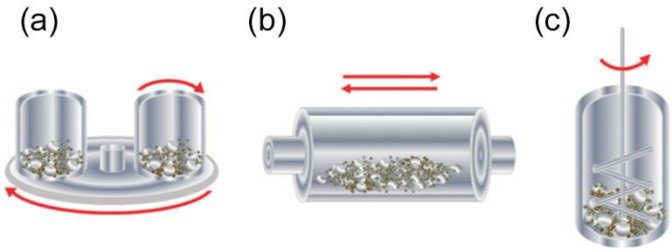

Figure 1.4

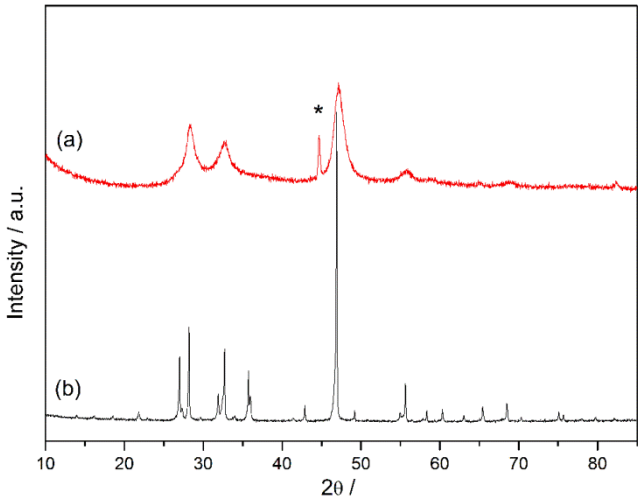

Figure 1.5

(a) (b)

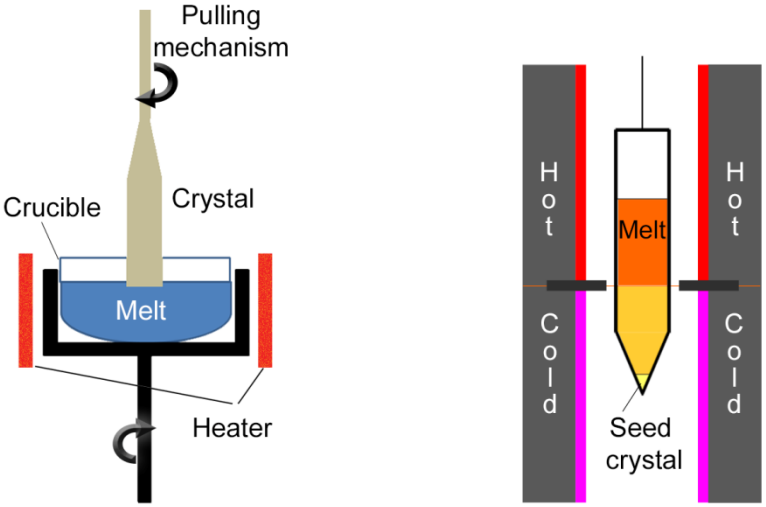

Figure 1.6

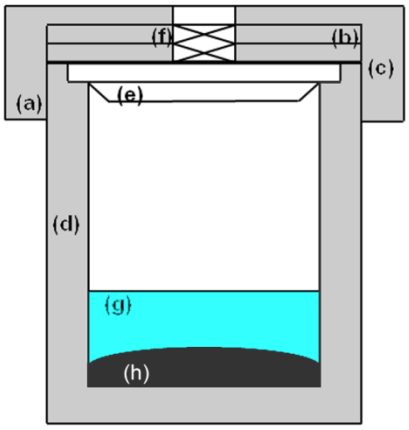

Figure 1.7

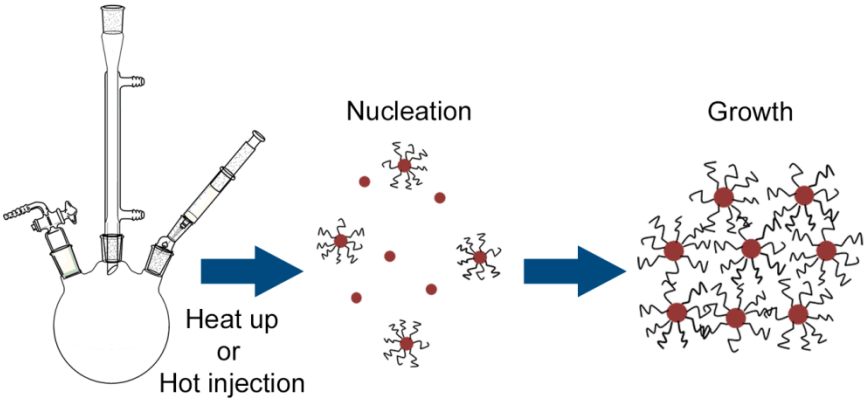

Figure 1.8

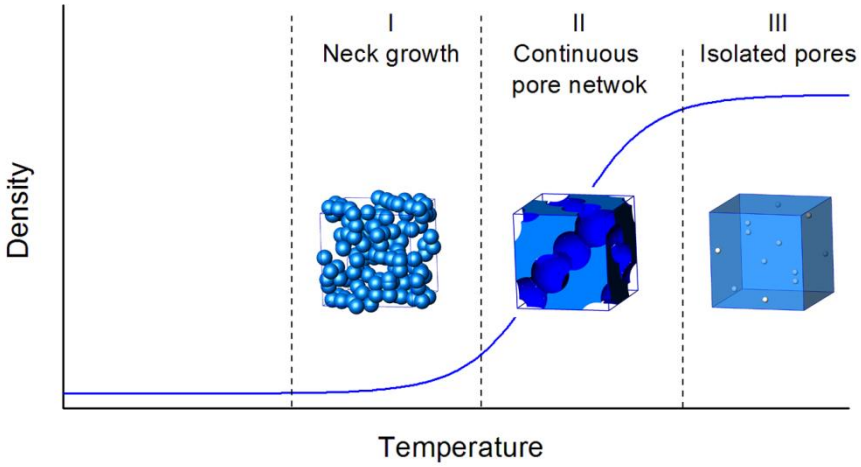

Figure 1.9

(a) (b)

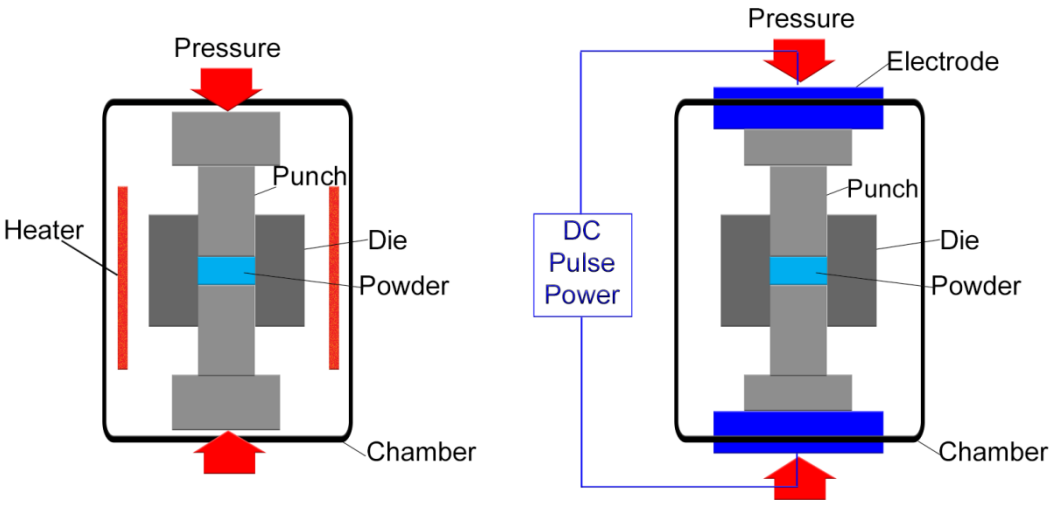

Figure 1.10

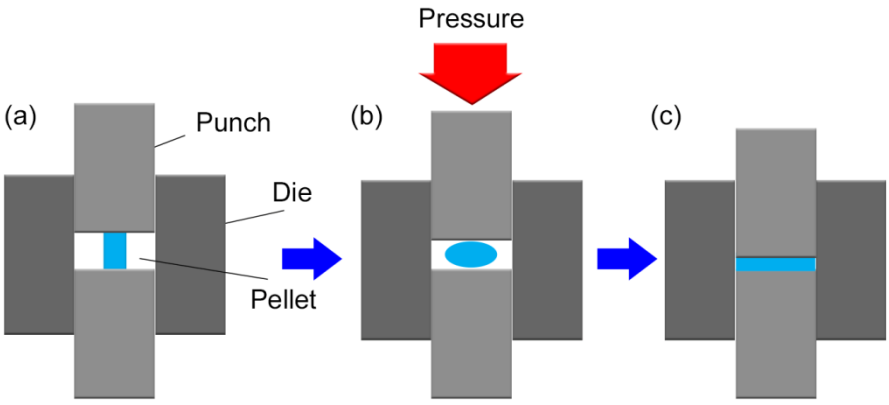

Figure 1.11

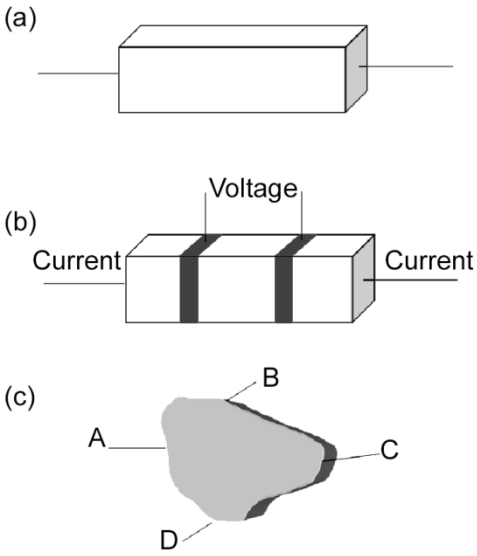

Figure 1.12

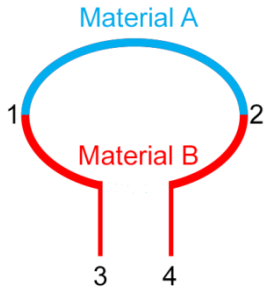

Figure 1.13

(a) (b)

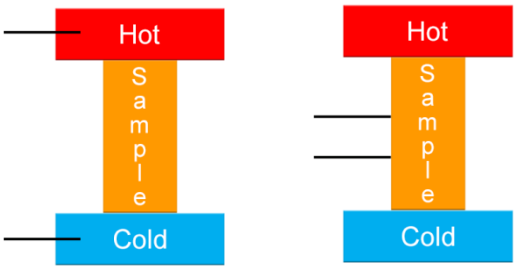

Figure 1.14

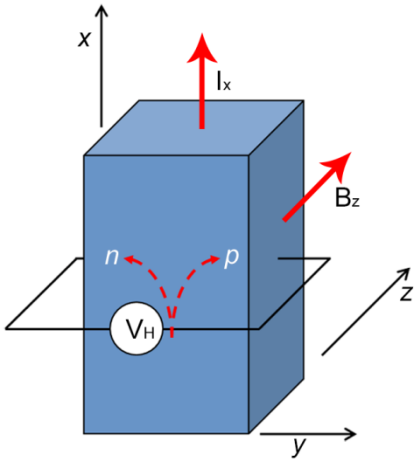

Figure 1.15

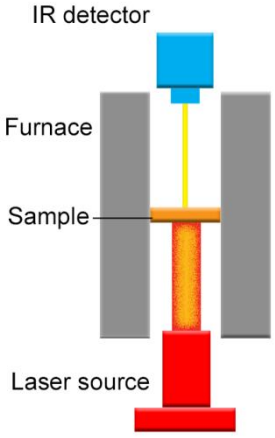

Figure 1.16

Table 1.1

Maximum operating temperatures for commonly used crucible materials.

Material	Temperature/K
Alumina (Al_2O_3)	2,000
Quartz/silica (SiO_2)	1,500
Boron nitride (BN)	1,173 in air 2,273 in Ar/N_2
Graphite (C)	673 in air 3,000 in Ar/N_2
Zirconia (ZrO_2)	2,300
Platinum	1,500
Tantalum	573 in air 1,700 in Ar/N_2
Zirconium	700 in air 1,700 in Ar/N_2

Table 1.2

Selected examples of thermoelectric materials prepared by mechanosynthesis. Key: PM = Planetary Mill; SM = Shaker mill; HP = Hot press; SPS = Spark-plasma sintering.

Material	Synthesis	Maximum ZT	Ref
$Si_{80}Ge_{20}P_2$	PM + HP	1.3 @ 1,173 K	37
$Bi_2Se_{0.15}Te_{2.85}$, doped with 0.07 wt% SbI_3	PM @ 400 rpm HP @ 723 K for 1 h annealed @ 723 K for 2 h	0.7 @ 300 K	38
$Tl_{0.02}Pb_{0.98}Te$	PM for 10-20 h HP	1.3 @ 673 K	40
$La_{3-x}Te_4$	SM for less than 24 h, HP @ 1,300 K	1.13 @ 1,273 K	39
$Ti_{0.95}Nb_{0.05}S_2$	PM @ 600 rpm for 48 h, SPS @ 1073 K for 30 min	0.3 @ 700 K	41
Cu_5FeS_4	PM @ 500 rpm for 40 h, HP @ 823 K for 30 min	0.55 @ 543 K	43
$Cu_{10.4}Ni_{1.6}Sb_4S_{13}$	PM @ 600 rpm for 20 h, SPS @ 753 K for 30 min	0.75 @ 700 K	42
TiNiSn	PM @ 300 rpm SPS @ 1,123 K for 10 min	0.32 @ 785 K	46
$CoSb_{2.75}Sn_{0.05}Te_{0.20}$	PM @ 400 rpm for 10 h, HP @ 873 for 30 min	1.13 @ 673 K	45
$Ce_{0.8}Fe_3CoSb_{12}$	PM @ 400 rpm for 10 h, HP @ 873 for 30 min	0.68 @ 773 K	44
$Ce_{0.5}Yb_{0.5}Fe_{3.25}Co_{0.75}Sb_{12}$	PM @ 400 rpm for 10 h, HP @ 873 for 30 min	0.93 @ 823 K	44
BiCuSeO	PM @ 500 rpm for 13 h, SPS @ 973 K for 5 min	0.5 @ 773 K	47

Table 1.3

Selected examples of single-crystal thermoelectric materials prepared using a molten flux.

Material	Flux	Flux removal	Ref
BiCuSeO	NaCl/KCl	Water	69,70
$A_xBa_{8-x}Al_{14}Si_{31}$ (A = Sr, Eu)	Al	Decanted, followed by 5 M NaOH	71
$Ca_3Co_2O_6$	K_2CO_3	Water	72
$Yb_{14}MnSb_{11}$	Sn	Centrifuge	73

Table 1.4

Selected examples of nanostructured thermoelectric materials prepared by solvothermal synthesis, together with the maximum figure of merit, *ZT* (when reported). Key: en = ethylenedieamine; PVP = polyvinylpyrrolidone; PEG = polyethylene glycol.

Material	Reagents	Solvent	*T*/K	Morphology	Maximum *ZT*	Ref
Bi_2Te_3	$Bi_2(C_2O_4)_3$ + Te	en	413	Flakes	-	85
Bi_2Te_3	Bi_2O_3 + TeO_2 + NaOH + PVP	Ethylene glycol	473	Nanoplates	-	86
$Bi_xSb_{2-x}Te_3$	$Bi(NO_3)_3{\cdot}5H_2O$ + $SbCl_3$ + Na_2TeO_3 + NaOH	Ethylene glycol	503	Nanoplates	1.2@320K	87
Bi_2Se_3	$Bi_2(C_2O_4)_3$ + Se	en	413	Flakes		85
Bi_2S_3	$Bi_2(C_2O_4)_3$ + S	en	413	Flakes	-	85
Bi_2S_3	$BiCl_3$ + thiourea	ethanol	413	Needles	-	96
PbTe	PbC_2O_4 + Te	en	413	Nanocubes	-	85
PbTe	$Pb(C_2H_3O_2)_2$ + Te + hydrazine + PEG + NaOH	water/ethanol	433	Nanoboxes	-	88
Cu_2Se	CuO + SeO_2 + NaOH + PVP	Ethylene glycol	503	Nanoplates	1.82@850K	89
$Sn_{1-x}Se$	$SnCl_2{\cdot}2H_2O$ + Se + NaOH	water	403	-	2.1@873K	90
$CoSb_3$	$CoCl_2$ + $SbCl_3$ + $NaBH_4$	ethanol	523	Granules	0.61@725K	91
$FeSb_2$	$Fe(CH_3COO)_2$ + $Sb(CH_3COO)_3$ + $NaBH_4$	ethanol	493	Polygonal	-	92

Table 1.5

Selected examples of thermoelectric materials prepared using a colloidal method, together with the maximum figure of merit, *ZT* (when reported). Key: R = reduction, T = thermal decomposition; PVP = poly-vinylpyrrolidone; TEG = tetra-ethylene glycol; OAm= oleylamine; TOP = trioctylphosphine; ODE = 1-octadecene; HDA = hexadecylamine; ODPA = octadecylphosphonic acid; EG= ethylene glycol; OA= oleic acid.

Material	Reagents	Surfactant/ ligands	Solvent	Reaction type	Maximum *ZT*	Ref
$CoSb_3$	$CoCl_2 \cdot 6H_2O + SbCl_3 + NaBH_4$	PVP	TEG	R	-	107
SnSe	bis[bis(trimethylsilyl) amino]tin(II) + TOP:selenium	TOP	OAm	T	-	115
SnSe	$SnCl_2 \cdot 2H_2O$ + NaOH + Se + $NaBH_4$	-	Water	R	-	116
Cu_2SnSe_3	CuCl + $SnCl_4 \cdot 5H_2O$ + SeO_2	HDA, ODPA	ODE	T	0.3@730 K	113
$Cu_2CdSnSe_4$	CuCl + CdO + $SnCl_4 \cdot 5H_2O$ + SeO_2	HDA, ODPA	ODE	T	0.71@685 K	114
$Bi_2Te_{3-x}Se_x$	$Bi(NO_3)_3 \cdot 5H_2O$ + Na_2SeO_3 + Na_2TeO_3 +KOH	PVP	EG	R	1.31@438 K	110
PbTe/PbS	1. PbO + TOP:Te 2. Thioacetamide	OA	ODE	T	1.07@700 K	111
PbS/Ag	1. PbO +S 2. $AgNO_3$ + $Fe(NO_3)_3 \cdot 9H_2O$	OA OLA	ODE	T	1.7@850 K	112

Table 1.6

Anisotropy ratio of the electrical (ρ, S) and thermal (κ) transport properties for selected thermoelectric materials at room temperature, determined from data for single crystals or highly textured samples. The subscripts || and ⊥ refer to in-plane and out-of-plane properties, respectively.

Material	$\rho_{\parallel}/\rho_{\perp}$	$S_{\parallel}/S_{\perp}$	$\kappa_{\parallel}/\kappa_{\perp}$	Reference
$Bi_{0.4}Sb_{1.6}Te_3$	0.34	0.96	2.44	16
SnSe	10	0.9	1.4	64
$Bi_{0.875}Ba_{0.125}CuSeO$	4	1	0.7	151
$MnSi_{1.73}$	0.13	0.5	1.7	153
TiS_2	~0.002	-[a]	1.6	152

[a] Due to the size of the single crystals, only in-plane measurements were reported for *S*.

Table 1.7

Seebeck coefficients, *S*, at room temperature for selected examples of metals and semiconductors.

Material	S/ μV K^{-1}	Ref
Pt	-5	179
Cu	+1.8	180
Ag	+1.5	180
Bi_2Te_3	+230	181
PbTe	+300	181

Table 1.8

Thermal conductivities, κ, at room temperature for selected materials

Material	κ/ W m^{-1} K^{-1}	Ref.
Silicon	124	197
Al_2O_3	36	196
Cu	398	196
SiO_2 (amorphous)	1.38	196
Bi_2Te_3	2.0	197
PbTe	2.3	197

Table 1.9

Commonly used methods for the measurement of thermal conductivity in bulk materials.

Approach	Method
Steady state	Absolute Comparative Radial heat flow Parallel conductance
Transient (frequency-domain)	Pulse power (Maldonado technique)
Transient (time-domain)	Hot wire Laser flash Transient plane source (hot disk)

References

1. D. M. Rowe, *Thermoelectrics Handbook: Macro to Nano*, ed. D. M. Rowe, CRC Press, Taylor and Francis, Boca Raton, 2006, Chapter 1

2. J. R. Sootsman, D. Y. Chung and M. G. Kanatzidis, *Angew. Chem. Int. Ed.*, 2009, **48**, 8616.

3. G. Tan, L.-D. Zhao and M. G. Kanatzidis, *Chem. Rev.*, 2016, **116**, 12123.

4. A. V. Powell, *J. Appl. Phys.*, 2019, **126**, 100901.

5. A. V. Powell and P. Vaqueiro, *Thermoelectric Materials and Devices*, ed. I. Nandhakumar, N. M. White and S. Beeby, *RSC Energy Environ. Ser.*, 2017, **17**, 27.

6. K. Koumoto, Y. Wang, R. Zhang, A. Kosuga and R. Funahashi, *Annu. Rev. Mater. Res.*, 2010, **40**, 363.

7. S. D. N. Luu and P. Vaqueiro, *J. Materiomics*, 2016, **2**, 131.

8. L.-D. Zhao, J. He, D. Berardan, Y. Lin, J.-F. Li, C.-W. Nan and N. Dragoe, *Energy Environ. Sci*., 2014, **7**, 2900.

9. H. Kleinke, *Chem. Mater.*, 2010, **22**, 604.

10. M. Christensen, S. Johnsen and B. B. Iversen, *Dalton Trans.*, 2010, **39**, 978.

11. W. G. Zeier, J. Schmitt, G. Hautier, U. Aydemir, Z. M. Gibbs, C. Felser and G. J. Snyder, *Nat. Rev. Mater.*, 2016, **1**, 16032.

12. E. S. Toberer, A. F. May and G. J. Snyder, *Chem. Mater.*, 2010, **22**, 624.

13. P. Vaqueiro and A. V. Powell, *J. Mater. Chem.*, 2010, **20**, 9577.

14. J. D. Corbett, *Solid State Chemistry Techniques*, ed. A. K. Cheetham and P. Day, Clarendon Press, Oxford, 1995, Chapter 1.

15. U. Schubert and N. Hüsing, *Synthesis of Inorganic Materials*, Wiley, Weinheim, 2000, Chapter 1, pp. 5-15.

16. H. Scherrer and S. Scherrer, *Thermoelectrics Handbook: Macro to Nano*, ed. D. M. Rowe, CRC Press, Taylor and Francis, Boca Raton, 2006, Chapter 27.

17. S. Ballikaya, N. Uzar, S.Yildirim, J. R. Salvador and C. Uher, *J. Solid State Chem.*, 2012, **193**, 31.

18. K. Kurosaki, H. Muta, M. Uno and S. Yamanaka, *J. Alloys Comp.*, 2001, **315**, 234.

19. ASM Handbook Volume 3: Alloy Phase Diagrams, ed. H. Okamoto, M.E. Schlesinger, E.M. Mueller, ASM International, 2016.

20. S. Chen and Z. Ren, *Mater. Today*, 2016, **16**, 387.

21. K. Motzfeldt, *High Temperature Experiments in Chemistry and Materials Science*, First Edition. John Wiley & Sons, 2013, Chapter 2.

22. M. Oledzka, C.L. Lee, K.V. Ramanujachary and M. Greenblatt, *Mat. Res. Bull.*, 1997, **32**, 889.

23. G. S. Coyne, *The Laboratory Companion. A practical Guide to Materials Equipment, and Technique*, John Wiley & Sons, New Jersey, US, 2006, Chapter 8.

24. B. A. Cook and J. H. Harringa, *Thermoelectrics Handbook: Macro to Nano*, ed. D. M. Rowe, CRC Press, Taylor and Francis, Boca Raton, 2006, Chapter 19.

25. P. Baláž, M. Achimovičová, M. Baláž, P. Billik, Z. Cherkezova-Zheleva, J. M. Criado, F. Delogu, E. Dutková, E. Gaffet, F. Gotor, R. Kumar, I. Mitov, T. Rojac, M. Senna, A. Streletskii and K. Wieczorek-Ciurowam, *Chem. Soc. Rev.*, 2013, **42**, 7571.

26. S. L. James, C. J. Adams, C. Bolm, D. Braga, P. Collier, T. Friščići, F. Grepioni, K. D. M. Harris, G. Hyett, W. Jones, A. Krebs, J. Mack, L. Maini, A. G. Orpen, I. P. Parkin, W. C. Shearouse, J. W. Steed, D. C. Waddelli, *Chem. Soc. Rev.*, 2012, **41**, 413.

27. W. Ostwald, *Handbuch der Allgemeinen Chemie, Band 1*, Akademische Verlagsgesellschaft mbH, Leipzig, 1919, vol. 70.

28. IUPAC. Compendium of Chemical Terminology, 2nd ed. (the "Gold Book"). Compiled by A. D. McNaught and A. Wilkinson. Blackwell Scientific Publications, Oxford,1997. Online version (2019-) created by S. J. Chalk. ISBN 0-9678550-9-8. https://doi.org/10.1351/goldbook.

29. L. Takacs, *J. Met.*, 2000, **52**, 12.

30. M. C. Lea, *Am. J. Sci*., 1893, **46**, 413.

31. Y. Chen and J.S. Williams, *J. Alloys Comp.*, 1995, **217**, 181.

32. C. Suryanarayana, E. Ivanov and V.V. Boldyrev, *Mater. Sci. Eng. A*, 2001, **304-306**, 151.

33. P. Baláž, *Mechanochemistry in Nanoscience and Minerals Engineering*, Springer-Verlag, Berlin Heidelberg, 2008, Chapter 1, pp. 8-14.

34. F. P. Bowden and A. Yoffe, *Fast Reactions in Solids*, Butterworths Scientific Publications, London, 1958.

35. P. A. Thiessen, K. Meyer and G. Heinicke, *Grundlagen der Tribochemie*, Akademie-Verlag, Berlin, 1967.

36. L. Takacs, *Prog. Mater. Sci*, 2002, **47**, 355.

37. X. W. Wang, H. Lee, Y. C. Lan, G. H. Zhu, G. Joshi, D. Z. Wang, J. Yang, A. J. Muto, M. Y. Tang, J. Klatsky, S. Song, M. S. Dresselhaus, G. Chen, Z. F. Ren, *Appl. Phys. Lett.*, 2008, **93**, 193121.

38. J. Y. Yang, T. Aizawa, A. Yamamoto and T. Ohta, *J. Alloys Comp.*, 2000, **312**, 326.

39. A. F. May, J.-P. Fleurial and G. J. Snyder, *Phys. Rev. B*, 2008, **78**, 125205.

40. B. Yu, Q. Zhang, H. Wang, X. Wang, H. Wang, D. Wang, H. Wang, G. J. Snyder, G. Chen and Z. F. Ren, *J. Appl. Phys.*, 2010, **108**, 016104.

41. C. Bourgès, T. Barbier, G. Guélou, P. Vaqueiro, A. V. Powell, O. I. Lebedev, N. Barrier, Y. Kinemuchi and E. Guilmeau, *J. Eur. Ceram. Soc.*, 2016, **36**, 1183.

42. T. Barbier, S. Rollin-Martinet, P. Lemoine, F. Gascoin, A. Kaltzoglou, P. Vaqueiro, A, V. Powell and E. Guilmeau, *J. Am. Ceram. Soc*., 2016, **99**, 51.

43. G. Guélou, A.V. Powell and P. Vaqueiro, *J. Mater. Chem. C*, 2015, **3**, 10624.

44. J. Prado-Gonjal, P. Vaqueiro, C. Nuttall, R. Potter and A. V. Powell, *J. Alloys Comp.*, 2017, **695**, 3598.

45. J. Prado-Gonjal, M. Phillips, P. Vaqueiro, G. Min and A. V. Powell, *ACS Appl. Energy Mater.*, 2018, **1**, 6609.

46. M. Zou, J.-F. Li, B. Du, D. Liu and T. Kita, *J. Solid State Chem.*, 2009, **182**, 3138.

47. J. Wu, F. Li, T.-R. Wei, Z. Ge, F. Kang, J. He and J.-F. Li, *J. Am. Ceram. Soc*., 2016, **99** 507.

48. B. Poudel, Q. Hao, Y. Ma, Y. Lan, A. Minnich, B. Yu, X. Yan, D. Wang, A. Muto, D. Vashaee, X. Chen, J. Liu, M. S. Dresselhaus, G. Chen and Z. Ren, *Science*, 2008, **320**, 634.

49. X. Yan, A. Prokofiev, E. Bauer, P. Rogl, J. Bernardi and S. Paschen, *J. Alloys Comp.*, 2017, **725**, 783.

50. J. Li, Q. Tan, J.-F. Li, D.-W. Liu, F. Li, Z.-Y. Li, M. Zou and K. Wang, *Adv. Funct. Mater.*, 2013, **23**, 4317.

51. P. Baláž, E. Guilmeau, N. Daneu, O. Dobrozhan, M. Baláž, M. Hegedus, T. Barbier, M. Achimovičová, M. Kaňuchováf and J. Briančin, *J. Eur. Ceram. Soc.*, 2020, **40**, 1922.

52. P. Baláž, M. Hegedus, M. Baláž, N. Daneu, P Siffalovic, Z. Bujňáková, E. Tóthová, M. Tešínsky, M. Achimovičová, J. Briančin, E. Dutková, M. Kaňuchová, M. Fabián, S. Kitazono and O. Dobrozhan, *Prog. Photovolt. Res. Appl.*, 2019, **27**, 798.

53. G. Müller, *Cryst. Res. Technol.*, 2007, **42**, 1150.

54. P. Capper, *Springer Handbook of Electronic and Photonic Materials*, ed. S. Kasap, P. Capper, Springer, 2017, Chapter 12.

55. X. Liu, N. Fechler and M. Antonietti, *Chem. Soc. Rev*., 2013, **42**, 8237.

56. M. G. Kanatzidis, R. Pöttgen and W. Jeitschko, *Angew. Chem. Int. Ed.*, 2005, **44**, 6996.

57. M. G. Kanatzidis, *Chem. Mater.*, 1990, **2**, 353.

58. M. Binnewies, R. Glaum, M. Schmidt and P. Schmidt, *Chemical Vapor Transport Reactions*, De Gruyter, Berlin, Boston, 2012.

59. D. T. J. Hurle, *Crystal Pulling from the Melt*, Springer, Berlin , 1993.

60. T. E. Svechnikova, L. E. Shelimova, P. P. Konstantinov, M. A. Kretova, E. S. Avilov, V. S. Zemskov, C. Stiewe, A. Zuber and E. Muller, *Inorg. Mater.*, 2005, **41**, 1043.

61. N.V. Abrosimov, S.N. Rossolenko, V. Alex, A. Gerhardt and W. Schröder, *J. Crystal Growth*, 1996, **166**, 657.

62. E. S. Toberer, M. Christensen, B. B. Iversen and G. J. Snyder, *Phys. Rev. B*, 2008, **77**, 075203.

63. N. Keawprak S. Lao-ubol, C. Eamchotchawalit and Z. M. Sun, *J. Alloys Comp.*, 2011, **509**, 9296.

64. L.-D. Zhao, S.-H. Lo, Y. Zhang, H. Sun, G. Tan, C. Uher, C. Wolverton, V. P. Dravid and M. G. Kanatzidis, *Nature*, 2014, **508**, 373.

65. T. Caillat, J.-P. Fleurial and A. Borshchevsky, *J. Crystal Growth*, 1996, **166,** 722.

66. M. Yoshinaga, T. Iida, M. Noda, T. Endo and Y. Takanashi, *Thin Solid Films*, 2004, **461**, 86.

67. J. Wang, O. I. Lebedev, K. Lee, J.-A. Dolyniuk, P. Klavins, S. Bux and K. Kovnir, *Chem. Sci.*, 2017, **8**, 8030.

68. M. Tachibana, *Beginner's Guide to Flux Crystal Growth*, NIMS Monographs, Springer, Japan, 2017.

69. A. P. Richard, J. A. Russell, A. Zakutayev, L. N. Zakharov, D. A. Keszler and J. Tate, *J. Solid State Chem.*, 2012, **187**, 15.

70. S.-T. Dong, Y.-Y. Lv, B.-B. Zhang, F. Zhang, S. Yao, Y. B. Chen, J. Zhou, S.-T. Zhang, Z.-B. Gu and Y.-F. Chen, *CrysEngComm*, 2015, **17**, 6136.

71. C. L. Condron and S. M. Kauzlarich, *Inorg. Chem.*, 2007, **46**, 2556.

72. J. Takahashi, H. Yamane and M. Shimada, *Jpn. J. Appl. Phys.*, 2004, **43**, L331.

73. J. F. Rauscher, C. A. Cox, T. Yi, C. M. Beavers, P. Klavins, E. S. Toberer, G. J. Snyder and S. M. Kauzlarich, *Dalton Trans.*, 2010, **39**, 1055.

74. H. Schäfer, *Angew. Chem. Int. Ed.*, 1971, **10**, 43.

75. M. Koyano, J. Tanaka, K. Suekuni and T. Ariga, *J. Electron. Mater.*, 2012, **41**, 1317.

76. G. Y. Davydyuk, O. V. Parasyuk, Y. E. Romanyuk, S. A. Semenyuk, V. I. Zaremba, L. V. Piskach, J. J. Koziol and V. O. Halka, *J. Alloys Comp.*, 2002, **339**, 40.

77. M. Fardy, A. I. Hochbaum, J. Goldberger, M. M. Zhang and P. Yang, *Adv. Mater*., 2007, **19**, 3047.

78. S. N. Girard, X. Chen, F. Meng, A. Pokhrel, J. Zhou, L. Shi and S. Jin, *Chem. Mater.*, 2014, **26**, 5097.

79. J. R. Szczech, A. L. Schmitt, M. J. Bierman and S. Jin, *Chem. Mater.*, 2007, **19**, 3238.

80. G. Krabbes, W. Bieger, K.-H. Sommer, T. Söhnel and U. Steiner, Computer program TRAGMIN, version 5.0, IFW Dresden, University of Dresden, HTW Dresden, 2008. (https://www.htw-dresden.de/en/luc/forschung/chemieingenieurwesen/festkoerperchemie/translate-to-english-tragmin)

81. K. Byrappa and T. Adschiri, *Prog. Cryst. Growth Charact*., 2007, **53**, 117.

82. U. Schubert and N. Hüsing, *Synthesis of Inorganic Materials*, Wiley, Weinheim, 2000, Chapter 4, pp. 180-191.

83. J. Li, Z. Chen, R.-J. Wang and D. M. Proserpio, *Coord. Chem. Rev.*, 1999, **190-192**, 707.

84. W. S. Sheldrick and M. Wachhold, *Angew. Chem. Int. Ed.*, 1997, **36**, 206.

85. S.-H. Yu, J. Yang, Y.-S. Wu, Z.-H. Han, J. Lu, Y. Xie and Y.-T. Qian, *J. Mater. Chem.*, 1998, **8**, 1949.

86. G. Zhang, W. Wang, X. Lu and X. Li, *Cryst. Growth Des*., 2009, **9**, 151.

87. M. Hong, Z. G. Chen, L. Yang and J. Zou, *Nano Energy*, 2016, **20**, 144.

88. W. Wang, B. Poudel, D. Wang and Z. F. Ren, *Adv. Mater.*, 2005, **17**, 2110.

89. L. Yang, Z.-G. Chen, G. Han, M. Hong, Y. Zou and J. Zou, *Nano Energy*, 2015, **16**, 367.

90. W. Wei, C. Chang, T. Yang, J. Liu, H. Tang, J. Zhang, Y. Li, F. Xu, Z. Zhang and J.-F. Li, *J. Am. Chem. Soc.*, 2018, **140**, 499.

91. J. L. Mi, T. J. Zhu, X. B. Zhao and J. Ma, *J. App. Phys.*, 2007, **101**, 054314.

92. A. Datta and G. S. Nolas, *Eur. J. Inorg. Chem.*, **2012**, 55.

93. J. W. Thomson, K. Nagashima, P. M. Macdonald and G. A. Ozin, *J. Am. Chem. Soc.*, 2011, **133**, 5036.

94. R. MacColl and S. Windwer, *J. Phys. Chem.*, 1970, **74**, 1261.

95. C. Wu, S.-H. Yu, S. Chen, G. Liu and B. Liu, *J. Mater. Chem.*, 2006, **16**, 3326.

96. S. H. Yu, Y. T. Qian, L. Shu, Y. Xie, L. Yang and C. S. Wang, *Mater. Lett.*, 1998, **35**, 116.

97. H. Li, X. Du, L. Cao, X. Guo and Z. Yuan, *J. Mater. Sci.*, 2020, **55**, 2905.

98. B. Wang, Y. Wang, S. Zheng, S. Liu, J. Li, S. Chang, T. An, W. Sun and Y. Chen, *J. Alloys Comp.*, 2019, **806**, 676.

99. G. Tang, J. Liu, J. Zhang, D. Li, K. H. Rara, R. Xu, W. Lu, J. Liu, Y. Zhang and Z. Feng, *ACS Appl. Mater. Interfaces*, 2018, **10**, 30558.

100. X. L. Shi, K. Zheng, M. Hong, W. D. Liu, R. Moshwan, Y. Wang, X.-L. Qu, Z. G. Chen and J. Zou, *Chem. Sci*., 2018, **9**, 7376.

101. X. Ji, P. Alboni, Z. Su, N. Gothard, B. Zhang, T. M. Tritt and J. W. Kolis, *Phys. Status Solidi RRL*, 2007, **1**, 229.

102. J. Xin, J. Yang, S. Li, A. Basit, B. Sun, S. Li, Q. Long, X. Li, Y. Chen and Q. Jiang, *Chem. Mater.*, 2019, **31**, 2421.

103. S. Ortega, M. Ibáñez, Y. Liu, Y. Zhang, M. V. Kovalenko, D. Cadavid and A. Cabot, *Chem. Soc. Rev.*, 2017, **46**, 3510.

104. J. Park, J. Joo, S. G. Kwon, Y. Jang and T. Hyeon, *Angew. Chem., Int. Ed.*, 2007, **46**, 4630.

105. B. L. Cushing, V. L. Kolesnichenko and C. J. O'Connor, *Chem. Rev.*, 2004, **104**, 3893.

106. C. Coughlan, M. Ibáñez, O. Dobrozhan, A. Singh, A. Cabot and K. M. Ryan, *Chem. Rev.*, 2017, **117**, 5865.

107. L. Yang, H. H. Hng, H. Cheng, T. Sun and J. Ma, *Mater. Lett.*, 2008, **62,** 2483.

108. C. B. Murray, D. J. Norris and M. G. Bawendi, *J. Am. Chem. Soc.*, 1993, **115**, 8706.

109. J. M. Lee, R. C. Miller, L. J. Moloney and A. L. Prieto, *J. Solid State Chem.*, 2019, **273**, 243.

110. Y. Liu, Y. Zhang, K. H. Lim, M. Ibáñez, S. Ortega, M. Li, J. David, S. Martí-Sánchez, K. M. Ng, J. Arbiol, M. V. Kovalenko, D. Cadavid and A. Cabot, *ACS Nano*, 2018, **12**, 7174.

111. M. Ibáñez, R. Zamani, S. Gorsse, J. Fan, S. Ortega, D. Cadavid, J. R. Morante, J. Arbiol and A. Cabot, *ACS Nano*, 2013, **7**, 2573.

112. M. Ibáñez, Z. Luo, A. Genc¸ L. Piveteau, S. Ortega, D. Cadavid, O. Dobrozhan, Y. Liu, M. Nachtegaal, M. Zebarjadi, J. Arbiol, M. V. Kovalenko and A. Cabot, *Nat. Commun.*, 2016, **7**, 10766.

113. M. Ibáñez, D. Cadavid, U, Anselmi-Tamburini, R. Zamani, S. Gorsse, W. Li, A. M. Lopez, J. R. Morante, J. Arbiol and A. Cabot, *J. Mater. Chem. A*, 2013, **1**, 1421.

114. M. Ibáñez, D. Cadavid, R. Zamani, N. García-Castelló, V. Izquierdo-Roca, W. Li, A. Fairbrother, J. D. Prades, A. Shavel, J. Arbiol, A. Pérez-Rodríguez, J. R. Morante and A. Cabot, *Chem. Mater.*, 2012, **24**, 562.

115. W. J. Baumgardner, J. J. Choi, Y.-F. Lim and T. Hanrath, *J. Am. Chem. Soc.*, 2010, **132**, 9519.

116. G. Han, S. R. Popuri, H. F. Greer, J.-W. G. Bos, W. Zhou, A. R. Knox, A. Montecucco, J. Siviter, E. A. Man, M. Macauley, D. J. Paul, W.-G. Li, M. C. Paul, M. Gao, T. Sweet, R. Freer, F. Azough, H. Baig, N. Sellami, T. K. Mallick and D. H. Gregory, *Angew. Chem. Int. Ed.*, 2016, **55**, 6433.

117. M. He, L. Protesescu, R. Caputo, F. Krumeich and M. V. Kovalenko, *Chem. Mater.*, 2015, **27**, 635.

118. M. Scheele, N. Oeschler, K. Meier, A. Koronowski, C. Klinke and H. Weller, *Adv. Funct. Mater.*, 2009, **19**, 3476.

119. Y. Liu, G. Garcia, S. Ortega, D. Cadavid, P. Palacios, J. Lu, M. Ibáñez, L. Xi, J. De Roo, A. M. Lopez, S. Martı-Sanchez, I. Cabezas, M. de la Mata, Z. Luo, C. Dun, O. Dobrozhan, D. L. Caroll, W. Zhang, J. Martins, M. V. Kovalenko, J. Arbiol, G. Noriega, J. Song, P. Wahnon and A. Cabot, *J. Mater. Chem. A*, 2017, **5**, 2592.

120. L. De Trizio and L. Manna, *Chem. Rev.*, 2016, **116**, 10852.

121. A. Sotelo, Sh. Rasekh, M. A. Torres, P. Bosque, M. A. Madre and J. C. Diez, *J. Solid State Chem.*, 2015, **221**, 247.

122. U. Schubert and N. Hüsing, *Synthesis of Inorganic Materials*, Wiley, Weinheim, 2000, Chapter 4, pp. 192-222.

123. A. E. Danks, S. R. Hall and Z. Schnepp, *Mater. Horiz.*, 2016, **3**, 91

124. K. F. Cai, E. Müller , C. Drašar and A. Mrotzek, *Mat. Sci. Eng. B*, 2003, **104**, 45.

125. Z. Xiong. X. Chen, X. Zhao, S. Bai, X. Huang and L. Chen, *Solid State Sci.*, 2009, **11**, 1612.

126. Y. Liu, Y. Lin, Z. Shi and C.-W. Nan, *J. Am. Ceram. Soc.*, 2005, **88**, 1337.

127. A. L. Hector, *Chem. Soc. Rev.*, 2007, **36**, 1745.

128. A. C. Pierre, *Introduction to Sol-Gel Processing*, Springer Nature Switzerland, 2020, Chapter 4.

129. S. L Brock, I. U. Arachchige and K. K. Kalebaila, *Comments Inorg. Chem.* 2006, **27**, 1.

130. M. Saleemi, M. S. Toprak, S. Li, M. Johnsson and M. Muhammed, *J. Mater. Chem.*, 2012, **22**, 725.

131. A. Khan, M. Saleemi, M. Johnsson, L. Han, N.V. Nong, M. Muhammed and M. S. Toprak, *J. Alloys Comp.*, 2014, **612**, 293.

132. S. Le Tonquesse, E. Alleno, V. Demange, V. Dorcet, L. Joanny, C. Prestipino, O. Rouleau and M. Pasturel, *J. Alloys Comp*., 2019, **796**, 176.

133. R. F. Walker, *J. Am. Ceram. Soc.*, 1955, **38**, 187.

134. S. L. Kang, *Sintering: densification, grain growth and microstructure*, Elsevier, Oxford, 2004, Chapter 5.

135. A. C. Reardon, *Metallurgy for the Non-Metallurgist*, ASM International, Ohio, 2nd Ed., 2011, Chapter 6, p. 135.

136. H. V. Atkinson and S. Davies, *Metall. Mater. Trans. A*, 2000, **31**, 2981.

137. A. D. LaLonde, T. Ikeda and G. J. Snyder, *Rev. Sci. Instrum.*, 2011, **82**, 025104.

138. S. Grasso, H. Yoshida, H. Porwal, Y. Sakka and M. Reece, *Ceram. Int.*, 2013, **39**, 3243.

139. M. Sokol, S. Kalabukhov, M.P. Dariel and N. Frage, *J. Eur. Ceram. Soc.*, 2014, **34**, 4305.

140. D. M. Hulbert, A. Anders, D. V. Dudina, J. Andersson, D. Jiang, C. Unuvar, U. Anselmi-Tamburini and A. K. Mukherjee, *J. Appl. Phys*., 2008, **104**, 033305.

141. O. Guillon, J. Gonzalez-Julian, B. Dargatz, T. Kessel, G. Schierning, J. Räthel and M. Herrmann, *Adv. Eng. Mater.*, 2014, **16**, 830.

142. R. Orrù, R. Licheri, A. M. Locci, A. Cincotti and G. Cao, *Mater. Sci. Eng. R Rep.*, 2009, **63**, 127.

143. J. E. Garay, *Ann. Rev. Mater. Res*., 2010, **40**, 445.

144. S. Grasso, Y. Sakka and G. Maizza *Sci. Technol. Adv. Mater.*, 2009, **10**, 053001.

145. D. Kenfaui, D. Chateigner, M. Gomina and J. G. Noudem, *J. Alloys Comp.*, 2010, **490**, 472.

146. M. H. Lee, J. H. Park, S.-D. Park, J.-S. Rhyee and M.-W. Oh, *J. Alloys Comp.*, 2019, **786**, 515.

147. C. Bourgès, Y. Bouyrie, A. R. Supka, R. A. R. Al Orabi, P. Lemoine, O. I. Lebedev, M. Ohta, K. Suekuni, V. Nassif, V. Hardy, R. Daou, Y. Miyazaki, M. Fornari and E. Guilmeau, *J. Am. Chem. Soc.* 2018, **140**, 2186.

148. M. Perez-Estébanez, M. Peiteado, A. C. Caballero, F. J. Palomares, M. Nygren and J. Isasi-Marín, *Bol. Soc. Esp. Ceram. V.*, 2016, **55**, 38.

149. M. Beekman, M. Baitinger, H. Borrmann, W. Schnelle, K. Meier, G. S. Nolas and Y. Grin, *J. Am. Chem. Soc*., 2009, **131**, 9642.

150. G. Dennler , R. Chmielowski, S. Jacob, F. Capet, P. Roussel, S. Zastrow, K. Nielsch, I. Opahle and G. K. H. Madsen, *Adv. Energy Mater.*, 2014, **4**, 1301581.

151. J. H. Sui, J. Li, J. Q. He, Y. L. Pei, D. Berardan, H. J. Wu, N. Dragoe, W. Cai and L. D. Zhao, *Energy Environ. Sci.*, 2013, **6**, 2916.

152 H. Imai, Y. Shimakawa and Y. Kubo, *Phys. Rev. B*, 2001, **64**, 241104R.

153. M. I. Fedorov and V. K. Zaitsev, *Thermoelectrics Handbook: Macro to Nano*, ed. D. M. Rowe, CRC Press, Taylor and Francis, Boca Raton, 2006, Chapter 31.

154. F. K. Lotgering, *J. Inorg. Nucl. Chem.*, 1959, **9**, 113.

155. X. Yan, B. Poudel, Y. Ma, W. S. Liu, G. Joshi, H. Wang, Y. Lan, D. Wang, G. Chen and Z. F. Ren, *Nano Lett.* 2010, **10**, 3373.

156. L. Hu, Y. Zhang, H. Wu, Y. Liu, J. Li, J. He, W. Ao, F. Liu, S. J. Pennycook, X. Zeng, *Adv. Funct. Mater.*, 2018, **28**, 1803617.

157. M. Mikami, E. Guilmeau and R. Funahashi, *J. Mater. Res.*, 2005, **20**, 2491.

158. Y. M. Belov, S. M. Maniakin and I. V. Morgunov, *Thermoelectrics Handbook: Macro to Nano*, ed. D. M. Rowe, Taylor & Francis, CRC Press, Boca Raton, 2006, Chapter 20.

159. L. D. Ivanova, L. I. Petrova, Y. U. I. Granatkina, V. S. Zemskov, O. B. Sokoov, S. Y. A. Skipidarov and N. I. Duvankov, *Inorg. Mater.*, 2008, **44**, 687.

160. D. Vasilevskiy, R. A. Masut and S. Turenne, *J. Electron. Mater.*, 2012, **41**, 1057.

161. M. Zehetbauer, H. P. Stüwe, A. Vorhauer, E. Schafler and J. Kohout, *Adv Eng. Mater.*, 2003, **5**, 33.

162. G. Rogl, A. Grytsiv, P. Rogl, N. Peranio, E. Bauer, M. Zehetbauer and O. Eibl, *Acta Mater.* 2014, **63**, 30.

163. F. Euler, *J. Appl. Phys.*, 1957, **28**, 1342.

164. C. C. Zhang, X. A. Fan, J. Hu, C. P. Jiang, B. Feng, Q. S. Xiang, G. Q. Li and Y. W. Li, *Adv. Eng. Mater.*, 2016, **18**, 1777.

165. K. A. Borup, J. de Boor, H. Wang, F. Drymiotis, F. Gascoin, X. Shi, L. Chen, M. I. Fedorov, E. Müller, B. B. Iversen and G. J. Snyder, *Energy Environ. Sci.*, 2015, **8**, 423.

166. J. J. Shen, L. P. Hu, T. J. Zhu and X. B. Zhao, *Appl. Phys. Lett.*, 2011, **99**, 124102.

167. T. C. Harman, *J. Appl. Phys.*, 1958, **29**, 1373.

168. E. Müller, C. Stiewe, D. M. Rowe and S.G.K. Williams, *Thermoelectrics Handbook: Macro to Nano*, Ed. D. M. Rowe, Taylor & Francis, CRC Press, Boca Raton, 2006, Chapter 26.

169. I.G. Austin and N.F. Mott, *Adv. Phys.*, 1969 **18**, 41.

170. N. F. Mott and E. A. Davis, *Electronic Processes in Non-Crystalline Materials*, Clarendon Press, Oxford, 1979.

171. G. S. Nolas, J. Sharp and H.S. Goldsmid, *Thermoelectrics: Basic principles and new materials developments*, Springer, Chapter 4.

172. T. M. Tritt, *Thermoelectrics Handbook: Macro to Nano*, ed. D. M. Rowe, Taylor & Francis, CRC Press, Boca Raton, 2006, Chapter 23.

173. H. Wang, W.D. Porter, H. Böttner, J. König, L. Chen, S. Bai, T. M. Tritt, A. Mayolet, J. Senawiratne, C. Smith, F. Harris, P. Gilbert, J. W. Sharp, J. Lo, H. Kleinke and L. Kiss, *J. Electron. Mater.*, 2013, **42**, 654.

174. L. J. van der Pauw, *Philips Res. Repts.*, 1958, **13**, 1.

175. ASTM Standard F76-86, *Standard method for measuring Hall mobility and Hall coefficient in extrinsic semiconductor single crystals*, in 1991 Annual Book of ASTM Standards (American Society for Testing Materials, Philadelphia, USA, 1991)

176. A. T. Burkov, A. Heinrich, P. P. Konstantinov, T. Nakama and K. Yagasaki, *Meas. Sci. Technol.*, 2001, **12**, 264.

177. J. Martin and G. S. Nolas, *Rev. Sci. Inst.*, 2016, **87**, 015105.

178. C. Wood, *Rep. Prog. Phys.*, 1988, **51**, 459.

179. J. P. Moore and R. S. Graves, *J. Appl. Phys.*, 1973, **44**, 1174.

180. N. Cusack and P. Kendall, *Proc. Phys. Soc.*, 1958, **72**, 898.

181. G. S. Nolas, J. Sharp and H.S. Goldsmid, *Thermoelectrics: Basic principles and new materials developments*, Springer, Chapter 5

182. P. M. Chaikin, *Organic Superconductivity*, ed. V. Z. Kresin and W. A. Little, Plenum, New York, 1990, p. 101-115.

183. R. H. Heikes and R. W. Ure, *Thermoelectricity*, Interscience, New York, 1961.

184. S Hébert, D. Berthebaud, R. Daou, Y. Bréard, D. Pelloquin, E. Guilmeau, F. Gascoin, O. Lebedev and A. Maignan, *J. Phys.: Condens. Matter*, 2016, **28,** 013001.

185. H. J. Goldsmid and J. W. Sharp, *J. Electron. Mater.*, 1999, **28**, 869.

186. Z. M. Gibbs, H.-S. Kim, H. Wang and G. J. Snyder, *Appl. Phys. Lett.*, 2015, **106**, 022112.

187. J. Martin, T. Tritt and C. Uher, *J. Appl. Phys.*, 2010, **108**, 121101.

188. J. Martin, *Meas. Sci. Technol.*, 2013, **24**, 085601

189. J. Martin, W. Wong-Ng and M. L. Green, *J. Electron. Mater.*, 2015, **44**, 1998.

190. E. Alleno, D. Bérardan , C. Byl, C. Candolfi, R. Daou, R. Decourt, E. Guilmeau, S. Hébert, J. Hejtmanek, B. Lenoir, P. Masschelein, V. Ohorodnichuk, M. Pollet, S. Populoh, D. Ravot, O. Rouleau and M. Soulier, *Rev. Sci. Instrum.*, 2015, **86**, 011301

191. W. D. Callister and D. G. Rethwisch, *Materials Science and Engineering: An Introduction*, Wiley, 10th Ed., US, 2018, Chapter 18.

192. E. H. Putley, *The Hall effect and related phenomena*, Butterworths, London, 1960.

193. K. A. Borup, E. S. Toberer, L. D. Zoltan, G. Nakatsukasa, M. Errico, J.-P. Fleurial, B. B. Iversen and G. J. Snyder, *Rev. Sci. Instrum.*, 2012, **83**, 123902.

194. D. W. Koon, A. A. Bahl and E. O. Duncan, *Rev. Sci. Inst.*, 1989, **60**, 275.

195. N. Z. Lupu, N. M. Tallan and D. S. Tannhauser, *Rev. Sci. Instrum.*, 1967, **38**, 1658.

196. M. A. White, *Properties of Materials*, Oxford University Press, New York, 1999, Chapter 8.

197. G. S. Nolas and H. J. Goldsmid, *Thermal conductivity: theory, properties and applications*, ed. T. M. Tritt, Springer, 2004, Chapter 1.4.

198. H.-S. Kim, Z. M. Gibbs, Y. Tang, H. Wang and G. J. Snyder, *APL Mater.*, 2015, **3**, 041506.

199. J. Goldsmid, *Introduction to thermoelectricity,* Springer Series in Material Science, Springer, Springer-Verlag Berlin Heidelberg 2010, Chapter 8.

200. D. Zhao, X. Qian, X. Gu, S. A. Jajja and R. Yang, *J. Electron. Packag.*, 2016, **138**, 040802.

201. T. M. Tritt and D. Weston, *Thermal conductivity: theory, properties and applications*, ed. T. M. Tritt, Springer, 2004, Chapter 2.1, pp. 187-202.

202. W. J. Parker, R. J. Jenkins, P. Butler and G. L. Abbott, *J. Appl. Phys.*, 1961, **32**, 1679.

203. R. D. Cowan, *J. Appl. Phys.*, 1963, **34**, 926.

204. L. M. Clark III and R. E. Taylor, *J. Appl. Phys*., 1975, **46**, 714.

205. H. Wang, W.D. Porter, H. Böttner, J. König, L. Chen, S. Bai, T. M. Tritt, A. Mayolet, J. Senawiratne, C. Smith, F. Harris, P. Gilbert, J. Sharp, J. Lo, H. Kleinke and L. Kiss, *J. Electron. Mater.*, 2013, **42**, 1073.

206. H. Wang, S. Bai, L. Chen, A. Cuenat, G. Joshi, H. Kleinke, J. König, H. W. Lee, J. Martin, M.-W. Oh, W. D. Porter, Z. Ren, J. Salvador, J. Sharp, P. Taylor, A. J. Thompson, and Y.C. Tseng, *J. Electron. Mater.*, 2015, **44**, 4482.

207. ASTM E1269-11(2018), Standard Test Method for Determining Specific Heat Capacity by Differential Scanning Calorimetry, ASTM International, West Conshohocken, PA, 2018

208. F. Thompson, *Phys. Educ.*, 2008, **43,** 396.

209. T.R. Wei, M. Guan, J. Yu, T. Zhu, L. Chen and X. Shi, *Joule*, 2018, **2**, 2183.

210. D. Vasilevskiy, J.-M. Simard, R. Masut and S. Turenne, *J. Electron. Mater.*, 2014, **44**, 1733.

211. C. H. Champness and P. C. Parekh, *Can. J. Phys*., 1965, **43**, 1589.

212. B. Kwon, S. H. Baek, S. Keun Kim and J.-S. Kim, *Rev. Sci. Instrum*., 2014, **85**, 045108.

213. D. Vasilevskiy, J.-M. Simard, T. Caillat, R. A Masut and S. Turenne, *J. Electron. Mater.*, 2016, **45**, 1540.

214. A. D. Downey, T. P. Hogan and B. Cook, *Rev. Sci. Instrum*., 2007, **78**, 093904.

215. M.E. Orazem and B Tribollet, *Electrochemical impedance spectroscopy*, John Wiley & Sons, Inc., Hoboken, New Jersey, 2008.

216. J. García-Cañadas and G. Min, *J. Appl. Phys.*, 2014, **116**, 174510.

217. B. Beltrán-Pitarch, J. Prado-Gonjal, A. V. Powell, P. Ziolkowski and J. García-Cañadas, *J. App. Phys.*, 2018, **124**, 025105.

218. B. Beltrán-Pitarch, J. Prado-Gonjal, A. V. Powell, F. Martínez-Julián and J. García-Cañadas, *J. Phys. Chem.*, 2019, **123**, 12608.